

## The Relationship between Precipitation and Lightning in Tropical Island Convection: A C-Band Polarimetric Radar Study

LAWRENCE D. CAREY AND STEVEN A. RUTLEDGE

*Department of Atmospheric Science, Colorado State University, Fort Collins, Colorado*

(Manuscript received 21 April 1999, in final form 10 November 1999)

### ABSTRACT

One of the primary scientific objectives of the Maritime Continent Thunderstorm Experiment was to study cloud electrification processes in tropical island convection, in particular, the coupling between ice phase precipitation and lightning production. To accomplish this goal, a C-band polarimetric radar was deployed in the Tropics (11.6°S, 130.8°E) for the first time, accompanied by a suite of lightning measurements. Using observations of the propagation-corrected horizontal reflectivity and differential reflectivity, along with specific differential phase, rain and ice masses were estimated during the entire life cycle of an electrically active tropical convective complex (known locally as Hector) over the Tiwi Islands on 28 November 1995. Hector's precipitation structure as inferred from these raw and derived radar fields was then compared in time and space to the measured surface electric field, cloud-to-ground (CG) and total lightning flash rates, and ground strike locations.

During Hector's developing stage, precipitating convective cells along island sea breezes were dominated by warm rain processes. No significant electric fields or lightning were associated with this stage of Hector, despite substantial rainfall rates. Aided by gust front forcing, a cumulus merger process resulted in larger, taller, and more intense convective complexes that were dominated by mixed-phase precipitation processes. During the mature phase of Hector, lightning and the surface electric field were strongly correlated to the mixed phase ice mass and rainfall. Merged convective complexes produced 97% of the rainfall and mixed-phase ice mass and 100% of the CG lightning. As Hector dissipated, lightning activity rapidly ceased.

As evidenced from the multiparameter radar observations, the multicell nature of Hector resulted in the continuous lofting of supercooled drops to temperatures between  $-10^{\circ}$  and  $-20^{\circ}\text{C}$  in discrete updraft cores during both the early and mature phases. The freezing of these drops provided instantaneous precipitation-sized ice particles that may have subsequently rimed and participated in thunderstorm electrification via the noninductive charging mechanism.

### 1. Introduction and motivation

Controversy still exists as to whether tropical convection can become significantly electrified to produce lightning while warm rain processes dominate storm microphysics or whether mixed-phase microphysics (involving ice in the presence of supercooled water) is required (e.g., Vonnegut 1994). Several laboratory studies (e.g., Takahashi 1978a; Jayaratne et al. 1983; Saunders et al. 1991; among others) of the noninductive charging (NIC) of graupel particles during rebounding collisions with ice crystals in the presence of supercooled cloud liquid water strongly support the latter argument. In the past, most conventional (not polarized) radar studies of tropical convection (Rutledge et al. 1992; Williams et al. 1992; Zipser and Lutz 1994; Petersen et al. 1996, 1999) have determined that suffi-

ciently large reflectivities (e.g.,  $\geq 30$  to  $40$  dBZ) must exist at temperatures below some threshold (e.g.,  $0^{\circ}$  to  $-20^{\circ}\text{C}$ ) for a specified period of time (typically on the order of 10 min) before strong electric fields and hence lightning can occur. These results are an extension of earlier radar and lightning research accomplished at midlatitudes that revealed a strong correlation between the areal distribution (the so-called Larsen area) of moderate reflectivity (e.g.,  $\geq 30$ – $45$  dBZ) at an arbitrary height in the mixed-phase zone and lightning (e.g., Larsen and Stansbury 1974; Stansbury and Marshall 1978; Marshall and Radhakant 1978). One possible interpretation of these observations is that graupel particles are a prerequisite for lightning, consistent with the NIC mechanism.

However, the presence of large precipitation-sized ice (i.e.,  $D \geq 1$  mm) is largely inferred from the temporal evolution of reflectivity at a given environmental temperature and cannot be conclusively determined with conventional radar. Moreover, a few anecdotal observations of warm cloud lightning have been reported (e.g., Foster 1950; Pietrowski 1960; Lane-Smith 1971)

---

*Corresponding author address:* Dr. Lawrence D. Carey, Department of Atmospheric Science, Colorado State University, Fort Collins, CO 80523-1371.  
E-mail: carey@olympic.atmos.colostate.edu

and, in one case, investigated in detail with cloud photography and 3-cm radar (Moore et al. 1960). More recently, dual-polarimetric radar observations that provide remotely sensed information on the size, shape, orientation, and thermodynamic phase of hydrometeors have been used to differentiate between millimeter-sized raindrops and precipitation-sized ice particles (e.g., Jameson 1985; Bringi and Hendry 1990; Jameson and Johnson 1990; Doviak and Zrnić 1993) and estimate the radar reflectivity associated with both rain and ice (e.g., Golestani et al. 1989; Balakrishnan and Zrnić 1990; see also appendix B).

The microphysical information inferred from polarimetric radar measurements have been correlated to electrical activity in subtropical and midlatitude convection. Goodman et al. (1988) was the first to use reflectivity and differential reflectivity to infer the presence of graupel and hail aloft during a rapid increase in the total lightning flash of an isolated storm in the vicinity of Huntsville, Alabama. Recently, Jameson et al. (1996), Ramachandran et al. (1996), French et al. (1996), and Bringi et al. (1997) employed polarimetric radar data to demonstrate that the onset of significant electrification in small, isolated Florida storms during the Convection and Precipitation/Electrification (CaPE) experiment was coincident with the freezing of supercooled raindrops at  $-7^{\circ}$  to  $-10^{\circ}\text{C}$  and the commencement of mixed-phase precipitation processes. Several multiparameter radar studies of High Plains hailstorms (Carey and Rutledge 1996; López and Aubagnac 1997; Carey and Rutledge 1998) have linked the evolution of cloud-to-ground (CG) and intracloud (IC) lightning flash rates to variations in graupel and hail production aloft.

The purpose of this study is to utilize polarimetric radar observations to further explore the hypothesis that *lightning production in tropical island convection is critically linked to ice processes in the mixed-phase region* via the NIC mechanism. During the Maritime Continent Thunderstorm Experiment (MCTEX; Keenan et al. 1994a), complete life cycle observations of thunderstorms over the Tiwi Islands (Bathurst and Melville Islands, which are centered at about  $11.6^{\circ}\text{S}$ ,  $130.8^{\circ}\text{E}$ ; see Fig. 1) were obtained with the Bureau of Meteorology Research Centre (BMRC) C-band (5.33 cm) dual-polarimetric radar (C-pol). These observations were carried out from 13 November to 10 December 1995. The BMRC C-pol observations are the *first comprehensive multiparameter radar observations of tropical convection in general and tropical island convection in particular*.

Earlier Doppler radar and lightning studies of convection in the vicinity of Darwin, Australia (Rutledge et al. 1992; Williams et al. 1992) confirmed the copious production of lightning in these storms and demonstrated the correlation between vertical reflectivity structure and lightning production in tropical convection. We extend these results in the present study by correlating the

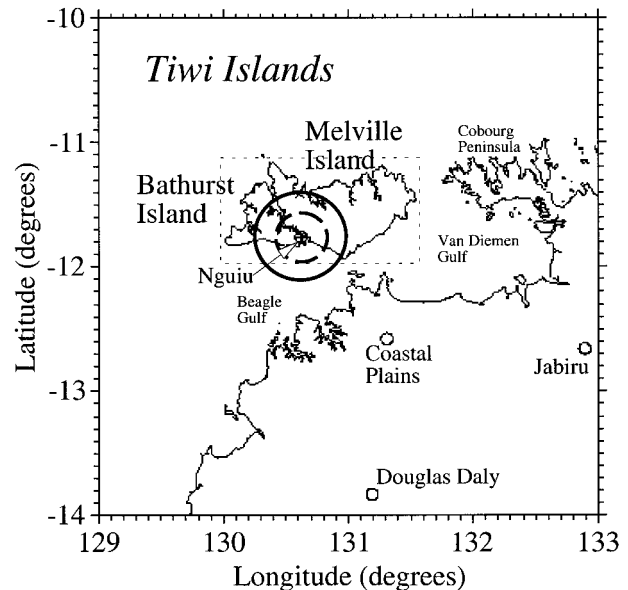


FIG. 1. A depiction of the radar and electricity/lightning instrumentation network during MCTEX. The BMRC C-pol radar is indicated by the + symbol. A flat plate antenna and shuttered field mill were collocated with the radar. The maximum operating range of the flat plate antenna (field mill) was approximately 40 km (20 km) as indicated by the solid (dashed) range ring around the C-pol radar. The ALDF network was composed of four sensors located at Nguiu, Coastal Plains, Jabiru, and Douglas Daly.

polarimetric radar-inferred production of ice in the mixed-phase region to the surface electric field as measured by a shuttered field mill, the total lightning flash rate as estimated from a flat plate antenna, and the CG lightning flash rate and ground strike locations as measured by a network of Advanced Lightning Direction Finders (ALDFs). With these results, we hope to *better understand cloud electrification and the correlation of lightning to the horizontal and vertical precipitation structure of tropical convection*. In particular, we investigate the role of the NIC mechanism in the electrification of and lightning production within tropical convection. We accomplish this goal by estimating the amount of graupel aloft in the mixed-phase zone with polarimetric radar. In addition, we explore the role of drop freezing in the production of significant graupel mass. As mentioned earlier, graupel is one of three key ingredients for the separation of charge via the NIC mechanism (e.g., Takahashi 1978a). The presence or absence of the other two key ingredients (supercooled cloud liquid water and cloud ice) are inferred indirectly from the vertical structure and temporal evolution of the precipitation field.

In section 2, an overview of radar and lightning data and analysis methods is given. More details regarding the determination of cloud electrical properties, the partitioning of reflectivity into rain and ice components using polarimetric radar data, and the estimation of ice and rain mass/rate are presented in appendixes A–D.

Results from polarimetric radar and electrical observations of intense tropical convection are discussed in section 3. Last, we summarize the results in section 4.

## 2. Data and analysis method

The MCTEX instrumentation network for electrification and lightning studies is depicted in Fig. 1. The BMRC C-band polarimetric radar (C-pol, 5.33 cm; Keenan et al. 1998) was located in the settlement of Nguiu on Bathurst Island (11.8°S, 130.6°E). Collocated at the radar was a flat plate antenna (e.g., Uman 1987) that measured the total lightning flash rate (total = IC + CG) within about 35–40 km; a shuttered field mill (Malan and Schonland 1950) for estimating the surface electric field and total lightning flash rate within 15–20 km; and an ALDF (e.g., Krider et al. 1976) for measuring the azimuth, signal power, polarity, and arrival time of lightning radio sources associated with cloud-to-ground return strokes within 600 km. Three other ALDF stations were positioned in a triangular configuration over the northern territory of Australia (at Coastal Plains, Douglas Daly, and Jabiru), completing the ALDF network (see Fig. 1). Details regarding the determination of cloud electrical properties (e.g., surface electric field, total lightning flash rate, CG lightning flash rate, and ground stroke location) from the above three instruments are presented in appendix A.

On 28 November 1995, the C-pol radar collected full volumetric scans of island convection in polarimetric mode every 4–15 min. Polarimetric variables utilized in this study include horizontal reflectivity ( $Z_h$ ), differential reflectivity ( $Z_{dr}$ ), and total differential phase ( $\Psi_{dp}$ ). These variables were carefully edited and quality controlled to remove any spurious data. Using a 13-sample (3.9 km) running mean, iterative filtering technique (Balakrishnan and Zrnić 1990; Hubbert and Bringi 1995), the differential propagation phase ( $\phi_{dp}$ ) and the specific differential phase ( $K_{dp}$ ) were estimated from  $\Psi_{dp}$ . The horizontal reflectivity and the differential reflectivity were then corrected for propagation effects in rain using  $\phi_{dp}$  (Bringi et al. 1990; Ryzhkov and Zrnić 1995a). For more details regarding polarimetric radar data editing, processing, and the correction of propagation effects at C band, see Carey et al. (2000). In addition, the difference reflectivity ( $Z_{dp}$ ) was calculated from attenuation corrected  $Z_h$  and differential attenuation corrected  $Z_{dr}$  according to the definition of Golestani et al. (1989). The reader is referred to several review papers and texts for formal definitions of these polarimetric variables and their applications (e.g., Bringi and Hendry 1990; Jameson and Johnson 1990; Doviak and Zrnić 1993). Finally, all of the processed and corrected polarimetric variables were interpolated to a Cartesian grid with 1-km horizontal and 0.5-km vertical resolution, using REORDER (Mohr 1986). The horizontal extent of these Cartesian grids covered the entire Tiwi Islands as depicted by the dashed box in Fig. 1. Since the beamwidth

of the C-pol radar is approximately 1°, there could be some smoothing of the data at ranges greatly in excess of 60 km.

In this study, we compare the lightning and surface electric field data to both polarimetric radar observables and radar-derived precipitation characteristics such as the mixed-phase precipitation ice mass, the precipitation liquid water content, and the rain mass flux. As described in appendix B, a technique for partitioning the measured horizontal reflectivity into  $Z_h(\text{rain})$  and  $Z_h(\text{ice})$  components using the  $Z_{dp}$  method (Golestani et al. 1989) at C band in tropical convection was developed and carefully evaluated using both C-pol and simulated radar data. As discussed in appendix C, estimates of rain mass ( $M_w$ ) and ice mass ( $M_i$ ) were then obtained by applying separate  $Z$ - $M$  relationships to the partitioned reflectivities. Finally, we calculated the rain mass flux ( $\text{kg s}^{-1}$ ) over the Tiwi using an optimal polarimetric radar rainfall algorithm utilizing propagation corrected  $Z_h$ ,  $Z_{dr}$ , and  $K_{dp}$ . These measurands were combined in such a way as to minimize error in the estimated rain rate at each grid point caused by variations in the drop size distribution and by observational error (e.g., Jameson 1991; Chandrasekar et al. 1993). Details of our optimal polarimetric rainfall algorithm can be found in appendix D.

Another goal of this study was to investigate the role of the cumulus merger process on the production of rainfall, mixed-phase graupel mass, and cloud-to-ground lightning since the merger process has implications for the manner in which tropical island convective systems are parameterized in large scale numerical models (e.g., Simpson et al. 1980, 1993). For the purposes of comparison with Simpson et al. (1993), we define a merger as a consolidation of two previously separate echo features at the 25 dBZ reflectivity isopleth (i.e., roughly corresponding to a rain rate of  $1 \text{ mm h}^{-1}$ ). A reflectivity echo feature is deemed as a group of horizontally contiguous grid points that exceed the 25 dBZ threshold at the 2-km grid level and that are isolated from other such groups by grid points characterized by reflectivity that does not exceed the threshold. The algorithm of Rickenbach and Rutledge (1998) was utilized to locate 25-dBZ echo features. Mergers between convective features were then identified by manual analysis. The rain mass flux of each feature was determined using the polarimetric rain-rate equations in appendix D. The number of cloud-to-ground lightning flashes associated with each feature was determined manually using a loop of ground strikes overlaid on the echo features. The mixed phase (5–11 km or 0° to –40°C) graupel mass, calculated using (C1)–(C4), was integrated in the vertical at each  $x$ - $y$  location in the grid. The Rickenbach and Rutledge (1998) feature identification technique was then applied to the integrated mixed-phase graupel mass. The features of mixed-phase graupel mass were then manually associated with the 25-dBZ reflectivity features at 2 km. In this manner, we were able to determine the echo area, rainfall, mixed-phase graupel

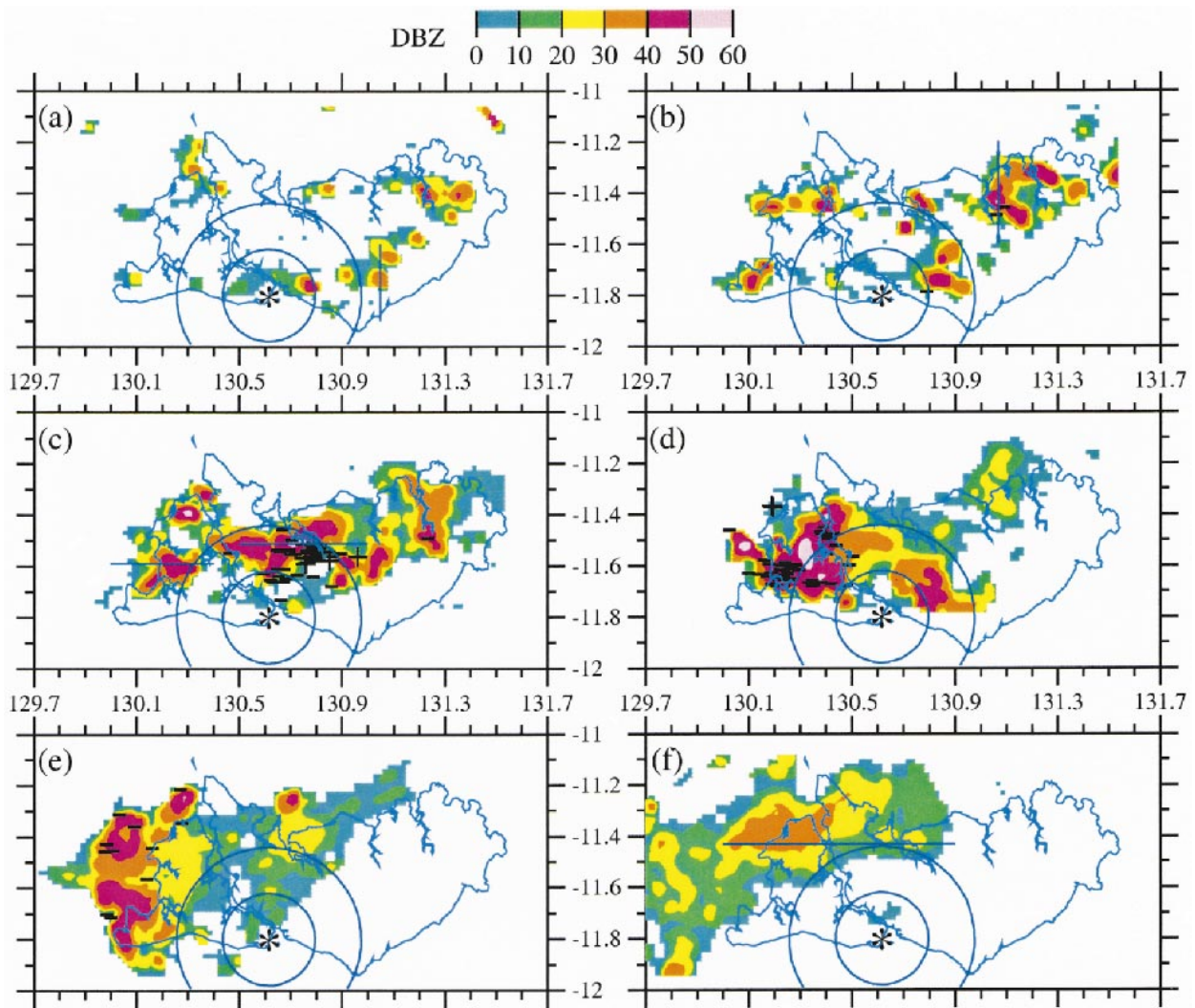


FIG. 2. Evolution of the horizontal reflectivity (dBZ) at 2-km altitude over the Tiwi Islands on 28 Nov 1995 at (a) 0216, (b) 0315, (c) 0416, (d) 0514, (e) 0614, and (f) 0715 UTC. The reflectivity is color shaded as shown. The radar location is indicated by a \* symbol and the flat plate (field mill) operating range ring at 40 km (20 km) is shown. The CG lightning flash locations during a 10-min period centered on the radar time are depicted. The black - (+) symbol indicates a negative (positive) polarity ground flash. The solid lines in Figs. 2a,b,c,d depict the planes of the vertical cross sections in Figs. 3–6.

mass, and cloud-to-ground lightning associated with every “single echo” and “merged echo” of the 28 November 1995 Hector.

### 3. Results and discussion

#### a. Overview of storm precipitation structure

The Hector event on 28 November 1995 was extremely intense from both a radar and lightning perspective. Echo tops (0 dBZ) reached to over 20 km while the 30-dBZ isosurfaces penetrated over 18 km. Maximum rainfall rates estimated by the C-pol radar exceeded  $150 \text{ mm h}^{-1}$  and observed reflectivities in the most intense cells surpassed 60 dBZ. At peak intensity, the convection spanned across the entire extent of both islands with

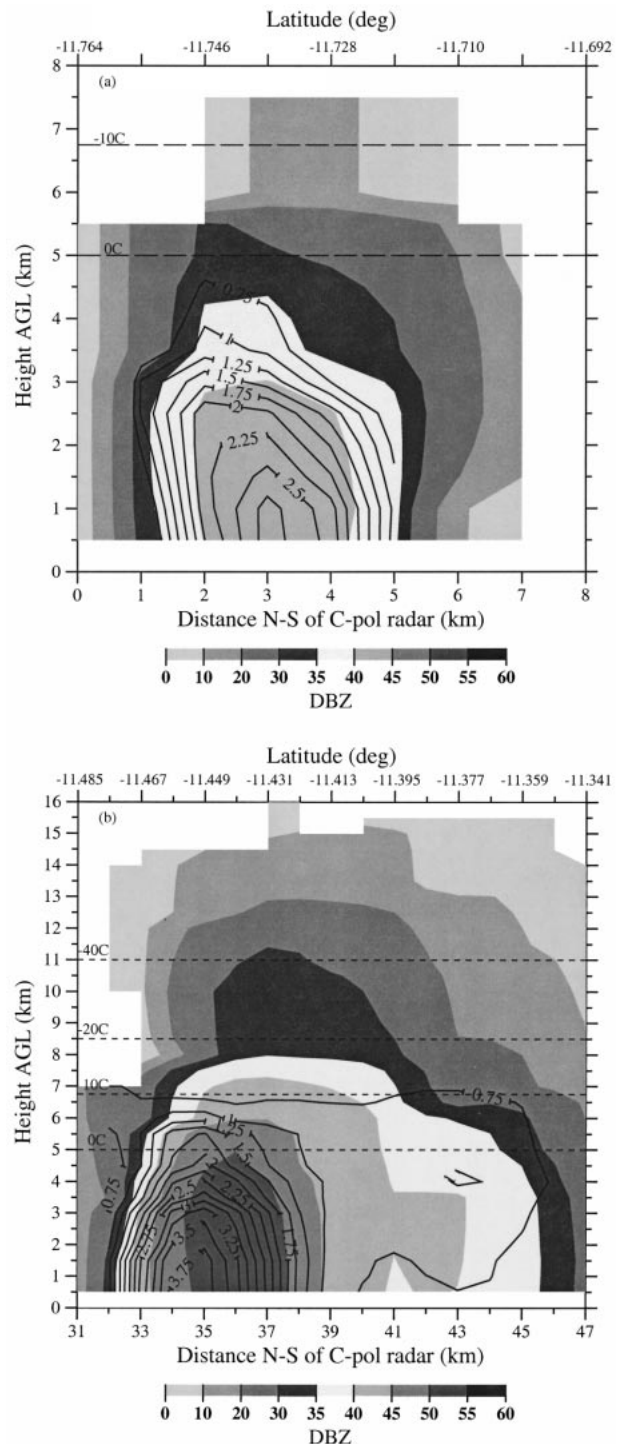
over 100 km of contiguous radar echo with reflectivities in excess of 30 dBZ along an east–west oriented line (at 2 km; Figs. 2c–d). Averaged over 1-min periods, the cloud-to-ground and total lightning flash rates peaked at 11 and  $60 \text{ min}^{-1}$ , respectively. Since this event is comparable to some of the most intense island thunderstorms observed in the region prior to MCTEX (Keenan et al. 1990, 1994b; Rutledge et al. 1992; Williams et al. 1992), it is considered to be an ideal case for studying the coevolving precipitation and lightning characteristics of deep island convection.

Precipitating convection lasted for 7 h (0130–0830 UTC or 1100–1800 local; all times hereafter will be referenced in UTC) in this case. By 0215, initial cumulonimbi were focused along two sea breeze fronts

(Keenan et al. 1994b; Carbone et al. 2000) occurring along the northern and southern coasts of both islands (Fig. 2a). Although there was no observed CG lightning over the islands, no lightning (IC or CG) detected by the flat plate antenna within 40 km of the radar, and no significant surface electric fields near the radar at this time, peak reflectivities and rain rates reached up to 55 dBZ and  $70 \text{ mm h}^{-1}$ , respectively. As shown in Fig. 3a, most convection was single celled with typical diameters on the order of 5–10 km and echo tops less than 8 km in height. The vertical extent of the 35-dBZ reflectivity and 1-dB differential reflectivity contours were limited to below the environmental freezing level at 5 km, suggesting that collision-coalescence dominated precipitation processes in most cells across the island. The most organized convection existed in extreme eastern Melville Island (e.g., see  $11.4^\circ\text{S}$ ,  $131.3^\circ\text{E}$ , Fig. 2a) where several cells had merged into a small convective complex on the order of 30 km wide. This merger was the result of the collision of a gust front with existing cumulus convection along the sea breeze front. This merger process is quite common over the Tiwi Islands (e.g., Keenan et al. 1994b; Carbone et al. 2000).

By 0315 (Fig. 2b), several cell mergers had occurred along both sea breeze fronts. Two of these complexes ( $11.8^\circ\text{S}$ ,  $130.8^\circ\text{E}$ ;  $11.45^\circ\text{S}$ ,  $131.1^\circ\text{E}$ ) were producing cloud-to-ground lightning at this time. The flat plate antenna measured total lightning flash rates of  $1\text{--}2 \text{ min}^{-1}$ , probably associated with the CG lightning producing complex to the east-northeast of the radar over southern Melville Island. The largest of the two CG lightning producing mergers, over northeastern Melville Island, produced the first detected ground flash earlier at 0300. The vertical structure of this complex (Fig. 3b) is in sharp contrast to that of the earlier single cell, which produced no CG lightning (Fig. 3a). Echo tops (0 dBZ) in the CG yielding complex exceeded 16 km. The 0.75-dB differential reflectivity contour and the 35-dBZ isopleth extended to 7 and 8 km, respectively. This implies that supercooled raindrops existed in the  $0^\circ$  to  $-10^\circ\text{C}$  region and that large precipitation-sized ice, most likely in the form of frozen drops and/or graupel, resided above the height of the  $-10^\circ\text{C}$  isotherm.

As a result of several cell mergers between 0315 and 0415, widespread deep convection stretched along an east-west line over both islands with the bulk of the activity over Melville Island (Fig. 2c). Associated with this explosive development of intense convection, the total lightning flash rate within 40 km of the radar increased from just a few to more than 30 flashes  $\text{min}^{-1}$ . In addition, the field mill detected the first significant electric field and multiple transients characteristic of lightning during this period. Cloud-to-ground lightning activity increased rapidly over Melville Island and at-



tained a relative maximum<sup>1</sup> of 5 flashes  $\text{min}^{-1}$  by 0415 (e.g., see Fig. 8). Interestingly, despite the widespread nature of significant convection ( $Z_h \geq 30$  dBZ) at 2 km, the overwhelming majority of ground discharges were confined to a relatively small region over western Melville Island near the northern coast (11.55°S, 130.8°E). For instance, note the complete absence of CG lightning over Bathurst Island up to and including 0415 (Figs. 2a–c).

In order to highlight the microphysical differences between convection that yields CG lightning and convection that does not, we present vertical cross sections of  $Z_h$ ,  $Z_{dr}$ , and  $K_{dp}$  through radar echo over Melville (Fig. 4a) and Bathurst (Fig. 4b) Islands. First, the storms over Melville Island (18.5-km echo tops) were significantly taller than those above Bathurst Island (13-km tops) at this time. The 35-dBZ echo height extended through the entire depth of the mixed phase region over Melville Island (roughly up to 11 km where  $T = -40^\circ\text{C}$ ). On the other hand, the 35-dBZ height did not penetrate the height of the  $-10^\circ\text{C}$  isotherm over Bathurst Island (only up to 6.5 km). Significant values of differential reflectivity ( $\geq 1$  dB) and specific differential phase ( $\geq 1^\circ \text{km}^{-1}$ ) suggest that supercooled raindrops were being lofted above the  $-10^\circ\text{C}$  level in both cells (e.g., Illingworth et al. 1987; Jameson et al. 1996; Brangi et al. 1996, 1997; Blyth et al. 1997). However, in the convection over Melville Island, there was a large volume of echo characterized by significant reflectivities ( $\geq 35$  dBZ) and near-zero values of  $Z_{dr}$  and  $K_{dp}$  at temperatures colder than  $-5^\circ\text{C}$  (i.e., heights  $\geq 5.9$  km), which is indicative of the presence of large precipitation-sized ice. In contrast, most of the radar echo possessing significant reflectivities over Bathurst Island were also characterized by significant positive values of  $Z_{dr}$  and  $K_{dp}$ . This indicates that a large fraction of the precipitation mass above the freezing level over Bathurst Island was in liquid form. This is an example where the penetration of some reflectivity threshold (30–35 dBZ) above some temperature threshold ( $-7^\circ$  to  $-10^\circ\text{C}$ ) does not guarantee the dominance of graupel or frozen drop mass over rain mass.

To explore further the vertical precipitation structure at 0416, we utilized the methods outlined in appendix C to estimate the reflectivity weighted rain ( $M_w$ ) and graupel mass<sup>2</sup> ( $M_g$ ) using  $Z_h$  and  $Z_{dp}$  in these two convective cells characterized by markedly different microphysics and CG lightning properties. Vertical cross sections of  $M_w$ ,  $M_g$ , and  $Z_h$  (Figs. 5a,b) are presented

<sup>1</sup> Unless otherwise noted, the CG lightning flash rates were averaged over a typical radar volume time (e.g., 6–7 min).

<sup>2</sup> In this context, graupel mass ( $M_g$ ) is defined as the reflectivity weighted ice mass determined by the  $Z_{dp}$  method that is characterized by  $Z_h \geq 35$  dBZ. The actual ice hydrometeor types could be graupel, frozen drops, and/or large aggregates. See appendix C for details.

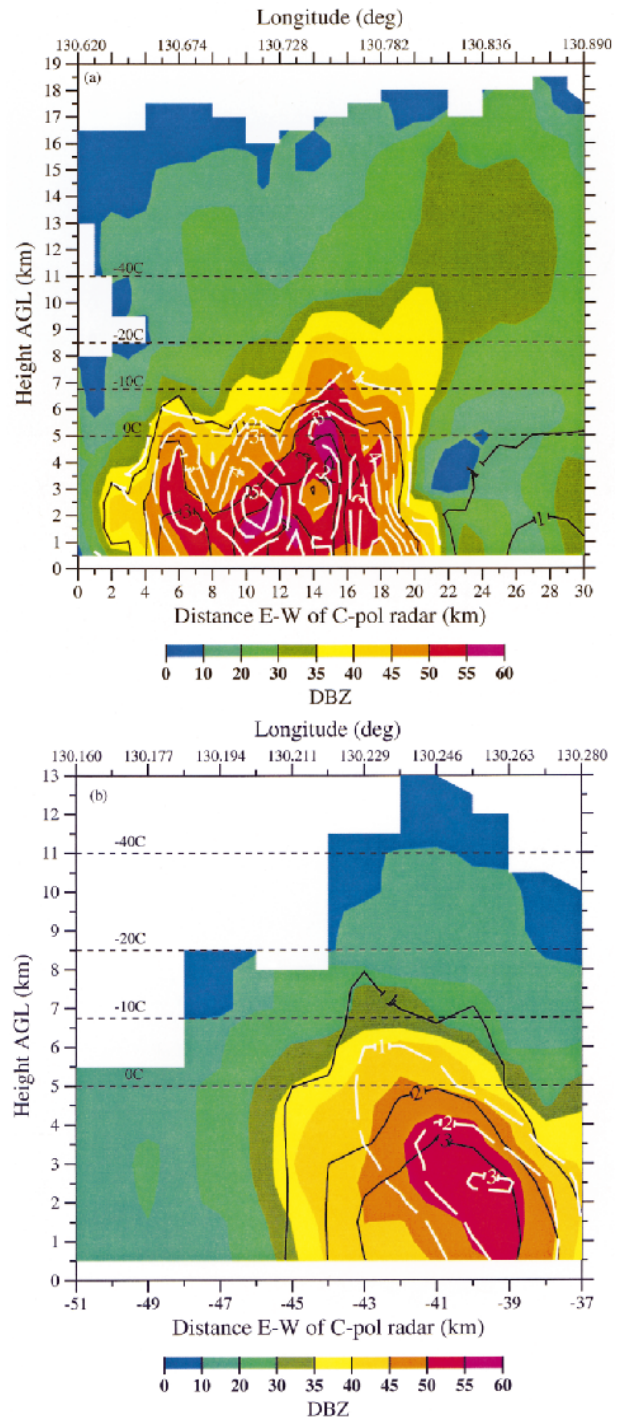


FIG. 4. East–west vertical cross section of  $Z_h$  (dBZ, color shaded as shown),  $Z_{dr}$  (dB, solid black contours), and  $K_{dp}$  ( $^\circ \text{km}^{-1}$ , dashed white contours) through (a) a CG lightning-producing convective complex over Melville Island (latitude = 11.51°S or  $y = 28$  km), and (b) a non-CG lightning-producing cell over Bathurst Island (latitude = 11.59°S or  $y = 19$  km) at 0416 UTC as depicted by the two solid lines in Fig. 2c.

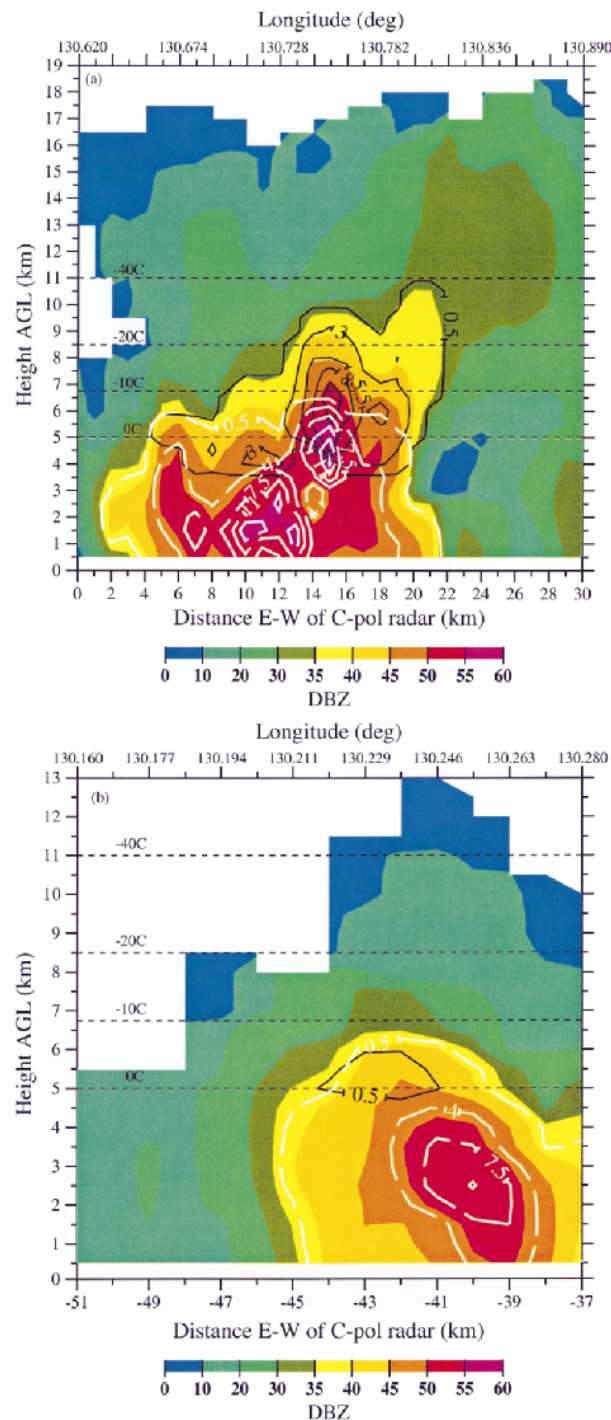


FIG. 5. Same as in Fig. 4 except of the polarimetric radar inferred graupel mass ( $M_g$ , solid black contours every  $2.5 \text{ g kg}^{-1}$  starting at  $0.5 \text{ g kg}^{-1}$ ) and the rain mass ( $M_w$ , dashed white contours every  $3.5 \text{ g kg}^{-1}$  starting at  $0.5 \text{ g kg}^{-1}$ ).

in the same planes as Figs. 4a,b respectively. The CG producing convective complex (Fig. 5a) had significant graupel mass throughout the entire mixed-phase region (5–11 km or  $0^\circ$  to  $-40^\circ\text{C}$ ) with a maximum in the  $0^\circ$

to  $-15^\circ\text{C}$  temperature zone. Note that the majority of the ground discharges occurring around 0416 were located beneath and just to the southeast of this peak in the ice mass aloft (cf. Figs. 2c and 5a). Contours of  $M_w$  indicate that supercooled raindrops were lofted to the height of  $-10^\circ\text{C}$ , where they likely froze and thus provided an immediate source of large precipitation ice for riming and charge separation via the NIC mechanism. The location of a maxima in the rain mass (4 km) located just below the peak graupel mass (6.5 km) strongly suggests that the freezing of supercooled raindrops is an important source of precipitation-sized ice in tropical convection.

As shown in Fig. 5b, the convection over Bathurst Island, which had not yielded a single CG lightning flash up to 0416, possessed a very different vertical structure of precipitation mass above 3.5 km ( $T < 8^\circ\text{C}$ ). From the surface to 3.5 km, both cells (Figs. 5a,b) had similar values of reflectivity and rain mass. In the Bathurst Island convection (Fig. 5b) the rain mass steadily decreased above 3.5 km and the peak in the graupel mass was an order of magnitude less than in the Melville Island complex. Indeed, very little graupel mass existed above the height of  $-10^\circ\text{C}$ . Figures 4b and 5b suggest that the Bathurst Island convection possessed sufficient updraft strengths to loft some supercooled drops to temperatures as low as  $-10^\circ\text{C}$ . However, the lack of significant graupel mass at and above the  $-10^\circ\text{C}$  level suggests that the updraft was insufficient to levitate precipitation (Atlas 1966) and thus allowed both large supercooled and frozen drops to fall back below the 5-km level. The lack of strong updrafts at and above the height of  $0^\circ\text{C}$  has been hypothesized to explain the dearth of lightning in tropical oceanic convection (Zipser and Lutz 1994; Petersen et al. 1999). In contrast, the Melville Island convection probably had strong enough updrafts ( $>6 \text{ m s}^{-1}$ ; Zipser and Lutz 1994) in the  $0^\circ$  to  $-20^\circ\text{C}$  to loft raindrops, balance frozen drops, and thus provide a source of large ice and supercooled cloud water for the NIC mechanism to be operative.

From 0415 to 0515, Hector moved westward with the most vigorous convection and CG activity now located over Bathurst Island (Fig. 2d). This complex reached its peak intensity between 0500 and 0515 with maxima in rainfall, ice mass aloft, CG and total lightning flash rates, and surface electric field. The merged complex continued to move westward from 0515 to 0615. A short (60 km) leading convective line resided off the coast of Bathurst Island followed by a narrow (30 km) trailing stratiform region (Fig. 2e). Cloud-to-ground lightning activity decreased rapidly during this period as the convective intensity decreased. By 0715, Hector began to take on a stratiform appearance in the horizontal (Fig. 2f) and vertical (Fig. 6) reflectivity structure (e.g., Steiner et al. 1995), ceased producing CG lightning, and generated about one IC lightning flash every 2 min. The intermittent bright band (Austin and Bemis 1950) structure in the reflectivity data at and below the melting

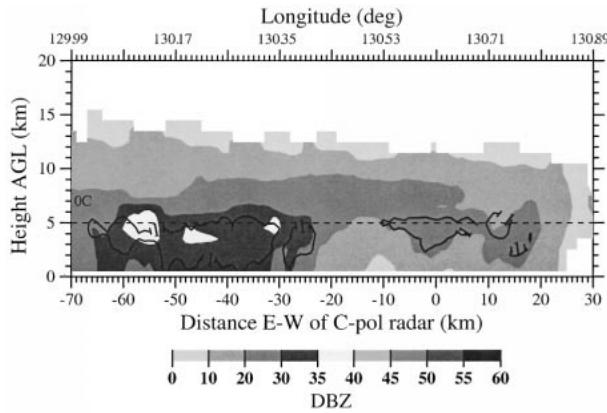


FIG. 6. East-west vertical cross section of  $Z_h$  (dBZ, shaded) and the 1-dB  $Z_{dr}$  contour through stratiform precipitation at 0715 UTC as depicted by the solid line in Fig. 2f.

layer and the peak in the differential reflectivity at and below the bright band (Zrnić et al. 1993) support the contention that Hector had taken on stratiform characteristics by 0715 (Fig. 6). The storm continued to weaken and move westward for the next 2 h. No further electrical activity was detected after 0740.

Using this overview of Hector's horizontal and vertical structure as background, we can explore the relationship between tropical island precipitation and lightning in detail.

*b. Relationship between cloud-to-ground lightning and precipitation*

As discussed in section 3a, the first few cloud-to-ground lightning flashes emanated from a convective complex over northeastern Melville Island from 0300 to 0315 (Figs. 2b, 3b). The microphysical evolution of this complex is revealed in two time-height cross sections<sup>3</sup> of raw (Fig. 7a) and derived (Fig. 7b) C-pol radar data.

In Fig. 7a, the evolution of  $Z_h$ ,  $Z_{dr}$ , and  $K_{dp}$  is depicted from the start of available polarimetric radar data (0215) to the end of the first flurry of CG lightning flashes associated with cell merger (0315). First, it is interesting to note that the 30- (35-) dBZ reflectivity contour remained at or above the height of the  $-20^{\circ}\text{C}$  ( $-10^{\circ}\text{C}$ ) level during the entire period, regardless of whether the storm was producing CG lightning, in contrast to the behavior of oceanic convection over the western Pacific warm pool (Petersen et al. 1996, 1999). There were two pulses in convective activity. No CG lightning was pro-

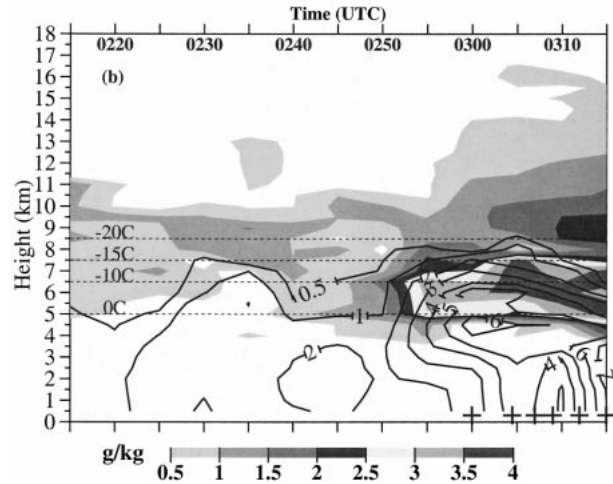
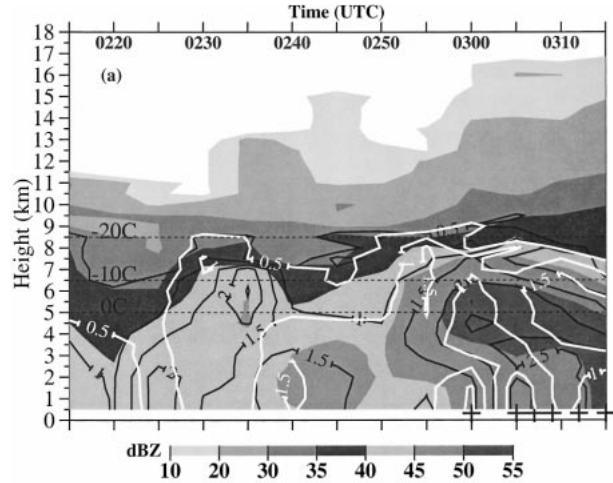


FIG. 7. Time-height cross section of the mean (a)  $Z_h$  (dBZ, shaded),  $Z_{dr}$  (dB, black contour), and  $K_{dp}$  ( $^{\circ}\text{km}^{-1}$ , white contour) and (b) radar-derived  $M_w$  ( $\text{g kg}^{-1}$ , black contour) and  $M_i$  ( $\text{g kg}^{-1}$ , shaded) through the convective complex over northeastern Melville Island, as depicted in Figs. 2c and 3b. This complex produced the first CG lightning flashes from 0300 to 0315 UTC. The time of each CG lightning flash is depicted by a + symbol along the bottom of the figure.

duced by the first pulse. The second pulse yielded the first six ground discharges.

The first convective pulse occurred from 0220 to 0240 with the most vigorous period from 0227 to 0237. Echo tops and the 40-dBZ echo height increased by 2.5 and 4.5 km, respectively, during this time period. The 0.5-dB ( $0.5^{\circ}\text{km}^{-1}$ ) contour for  $Z_{dr}$  ( $K_{dp}$ ) extended to the height of  $-20^{\circ}\text{C}$  during the first pulse, suggesting the presence of supercooled raindrops well above the freezing level. The second pulse was sustained for a longer period (0240–0315) and was more intense. For example, the second convective surge was characterized by larger values of reflectivity, differential reflectivity, and specific differential phase. Echo tops and the 40-dBZ echo height in the second pulse were higher, reaching up to 16.5 and 8.5 km, respectively. In the second pulse, sig-

<sup>3</sup> The analysis region for the time-height cross sections were based on subjectively determined three-dimensional boxes encompassing the complex in question. The quantities in Figs. 7a,b ( $Z_h$ ,  $Z_{dr}$ ,  $K_{dp}$ ,  $M_w$ ,  $M_i$ ) are averages of values in grid points that possess reflectivities within 3 dB of the maximum  $Z_h$  at each time.

nificant positive values of  $Z_{dr}$  and  $K_{dp}$ , indicative of raindrops, again extended to 8.5 km ( $-20^{\circ}\text{C}$ ). Due to the range of the convection in Figs. 7a,b (i.e., approximately 60 km), it is possible that the polarimetric variables were smeared a bit into the vertical plane. As a result, the  $-20^{\circ}\text{C}$  temperature level should be considered a lower limit to our estimate of the coldest temperature at which the presence of supercooled drops can be inferred. However, the resolution is more than sufficient to conclude that drops were lofted to the  $-10^{\circ}$  to  $-20^{\circ}\text{C}$  temperature zone.

The time–height evolution of the radar inferred rain ( $M_w$ ) and total ice ( $M_i$ ) mass for the same time period and convective complex is presented in Fig. 7b. Clearly, there was more ice mass above and rain mass below the freezing level in the second, CG producing pulse than in the first surge. The ice mass in the first convective pulse was typically between 0 and  $1.5\text{ g kg}^{-1}$  in the  $0^{\circ}$  to  $-20^{\circ}\text{C}$  region compared to a range of  $1.5\text{--}4\text{ g kg}^{-1}$  for the second surge. Inspection of the first pulse reveals that most of the precipitation mass in the  $0^{\circ}$  to  $-15^{\circ}\text{C}$  region was actually supercooled rain water or possibly partially frozen drops. As recently demonstrated by Smith et al. (1999), complete freezing of millimeter-sized drops can take a few minutes after nucleation. During this time required for freezing, we suggest that many of the drops fell back below the  $0^{\circ}\text{C}$  level without completely freezing due to a weak updraft in the  $0^{\circ}$  to  $-10^{\circ}\text{C}$  zone.

The temporal evolution of  $Z_h$ ,  $Z_{dr}$ ,  $K_{dp}$ , and  $M_w$  contours from 0230 to 0245 implies that much of the supercooled rain mass peak between  $0^{\circ}$  and  $-10^{\circ}\text{C}$  at the beginning of the pulse rained out by 0245 without contributing significantly to the ice mass aloft. Toward the end of the pulse at 0240, a relatively small amount of precipitation ice ( $M_i < 1.5\text{ g kg}^{-1}$ ) was produced via drop freezing. The lack of significant ice mass in the  $-10^{\circ}$  to  $-20^{\circ}\text{C}$  region where the negative charge region typically resides (e.g., Williams 1989) is consistent with the lack of CG lightning in the complex at this time, if the primary thunderstorm charging mechanism is NIC. More than likely, the updraft was not strong enough to balance the bulk of the rain mass above the height of the  $-10^{\circ}\text{C}$  level (Zipser and Lutz 1994; Petersen et al. 1996, 1999) and/or not of sufficient duration ( $<10\text{--}15$  min) to allow freezing, riming, significant charge separation, and lightning (Solomon and Baker 1994; Petersen 1997).

The second convective pulse immediately followed the freezing of the first, weaker pulse of supercooled drops above the  $0^{\circ}\text{C}$  level at 0240. It is possible that the release of latent heat during drop freezing provided enhanced buoyancy to this second pulse and thus contributed to a more vigorous updraft. Raindrops were once again lofted into the  $0^{\circ}$  to  $-20^{\circ}\text{C}$  region. This time, however, the lofted rain mass was significantly larger and the drops immediately began to freeze and produce significant ice mass aloft (Figs. 7a,b). The freezing was

much more rapid during the second pulse, perhaps as a result of ample residual cloud ice from prior convection initiating contact freezing (Cooper 1974). Yuter and Houze (1995) also concluded that increased concentrations of ice particles penetrated by new updrafts during the mature phase of a Florida storm observed during CaPE aided in the more rapid freezing of supercooled drops. During this pulse, the updraft was apparently vigorous enough and of sufficient duration to loft supercooled drops above  $-10^{\circ}\text{C}$ , balance millimeter-sized precipitation ice there, and allow the riming and electrification of ice via the NIC mechanism.

The first cloud-to-ground lightning flash occurred at 0300, within 5–10 min of the production of significant ice mass in the  $-10^{\circ}$  to  $-20^{\circ}\text{C}$  region (0250–0255). The occurrence of lightning about 10 min after the production of significant mixed-phase ice mass is consistent with prior studies of midlatitude and subtropical convection (e.g., Workman and Reynolds 1949; Dye et al. 1986; Goodman et al. 1988; Williams et al. 1989; Carey and Rutledge 1996; Jameson et al. 1996; Bringi et al. 1997) and tropical oceanic convection (e.g., Petersen et al. 1996). As seen in Figs. 7a,b, the complex continued to loft supercooled water into the  $0^{\circ}$  to  $-20^{\circ}\text{C}$  region after the first ground discharge. As a result, the production of ice mass, assumedly via drop freezing, continued to increase and then remained steady after 0305. The complex produced five additional cloud-to-ground lightning flashes before merging with another cell after 0315.

Although empirical and not conclusively causal, the evidence correlating the drop freezing process, production of precipitation sized ice, and subsequent electrification and lightning is fairly strong in this tropical island thunderstorm. In situ videosonde observations (T. Takahashi 1996, personal communication) taken during MCTEX confirm the common presence of supercooled raindrops and frozen drops in the mixed-phase region, even at temperatures as cold as  $-20^{\circ}$  to  $-25^{\circ}\text{C}$ . These in situ observations corroborate the importance of drop freezing in Hector's precipitation processes. The importance of drop freezing to the glaciating behavior of warm based clouds has long been known (e.g., Koenig 1963). The 1D bulk microphysical cloud modeling studies of Hector by Keenan et al. (1994b) and Petersen (1997) reveal the dominance of drop freezing over depositional and aggregational growth in the creation of large ice particles that can continue to grow via riming. In addition, the integrated cloud microphysical and electrical modeling results of Petersen (1997) suggest a critical role for frozen drops in the production of significant electric fields necessary for lightning. The role of drop freezing in subsequent cloud electrification and lightning production also has been demonstrated in the recent radar and/or aircraft studies of Jameson et al. (1996), French et al. (1996), Ramachandran et al. (1996), and Bringi et al. (1997) for subtropical convection, and by Petersen et al. (1999) for tropical oceanic convection.

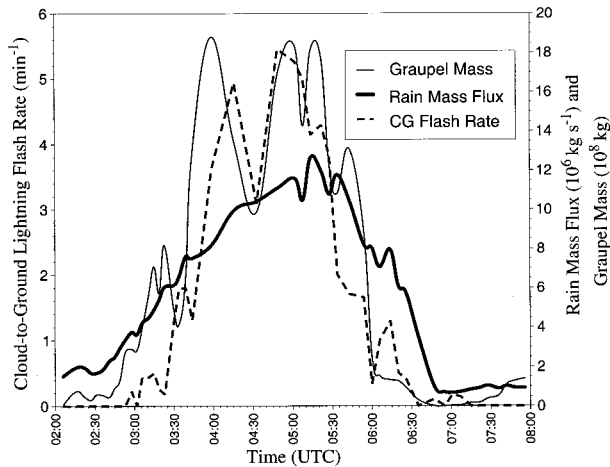


FIG. 8. Evolution of the CG lightning flash rate ( $\text{min}^{-1}$ ), rain mass flux ( $10^6 \text{ kg s}^{-1}$ ), and mixed-phase graupel mass ( $M_g$ ,  $10^8 \text{ kg}$ ) from 0200 to 0800 UTC over the Tiwi Islands. The CG lightning flash rate was averaged over the same temporal interval as the resolution of the available polarimetric radar data (i.e., 5–14 min).

With an understanding of how the production of mixed-phase ice mass is correlated to the production of ground discharges beneath a single convective complex, we now present the temporal evolution of the CG lightning flash rate, mixed phase graupel mass, and the rain mass flux over the entire Tiwi Islands for a 6-h period (0200–0800) during the complete life cycle of this case (Fig. 8). The rain mass flux broadly envelopes the period of significant ice mass and CG production. A nonnegligible amount of rain occurred prior to the first CG lightning flash at 0300. As discussed below, this pre-CG lightning rainfall is associated with primarily warm rain cumulonimbi (see Figs. 3a and 9). It is also interesting to note that the overall maximum and gradual decrease in the rain mass flux after 0515 lags the CG lightning flash rate and mixed-phase graupel mass by about 20 min. This temporal lag is probably associated with the gravitational settling time of the precipitation mass from the assumed position of the negative charge zone during CG lightning (about  $-10^\circ\text{C}$ ; Williams 1989) to the surface, as will be further demonstrated below.

The general trend of the CG lightning flash rate is well correlated with that of the graupel mass. For example, both parameters undulate in unison in Fig. 8; their maxima and minima consistently aligned. Maxima in the mixed-phase graupel mass typically preceded or were coincident in time with peaks in the cloud-to-ground lightning flash rate (at the available temporal resolution of 4–15 min). For example, note the relative maximum in the graupel mass aloft at 0359 that preceded the peak in the ground discharge rate at 0416 associated with the convective complex highlighted in Figs. 2c, 4a, and 5a. Other maxima in the CG lightning flash rate that were preceded by peaks in the graupel mass aloft by 10–30 min occurred at 0315, 0339, 0522,

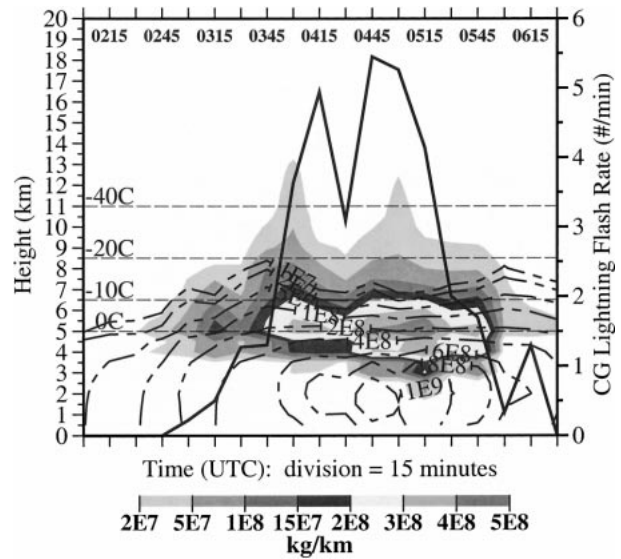


FIG. 9. Time–height cross section of the slab total graupel ice mass ( $\text{kg km}^{-1}$ , shaded) and rain mass ( $\text{kg km}^{-1}$ , dashed contour) from 0200 to 0630 UTC over the Tiwi Islands. The CG lightning flash rate ( $\text{min}^{-1}$ , solid line) during this period is repeated for direct comparison. Note that the CG lightning flash rate was averaged over the same temporal interval as the resolution of the available polarimetric radar data (i.e., 5–14 min).

and 0614. The one-lag correlation coefficient<sup>4</sup> between the graupel mass aloft and the CG lightning flash rate is very high ( $\rho = 0.9$ ).

The overall maxima in the CG lightning flash rate of  $5.5 \text{ min}^{-1}$  that occurred at 0449 was nearly coincident with a relative maxima in the graupel mass. The temporal resolution of the polarimetric radar data surrounding this peak was degraded to about 10–15 min so it is ambiguous as to whether this marks an actual break from the more typical trend (i.e., graupel maxima preceding CG maxima) or whether the C-pol radar did not resolve the actual time of the maxima in the graupel mass. Prior to 0430, there was one dominant complex producing CG lightning and graupel mass (e.g., Fig. 2c). From 0430 to 0530, there were multiple cells producing CG lightning and graupel mass aloft (e.g., Fig. 2d). Therefore, an alternate, physically based explanation for the change in behavior of graupel mass relative to CG lightning after 0430 is that the summation of graupel mass and CG lightning from multiple complexes in differing stages of their evolution masked the earlier trend.

The time–height cross section of the slab total<sup>5</sup> graupel and rain mass ( $\text{kg km}^{-1}$ ) in Fig. 9 further elucidate

<sup>4</sup> The CG lightning flash rate at time =  $T$  was correlated to the lagged graupel mass at time =  $(T - \tau)$  where  $\tau = 7 \text{ min}$  in the mean.

<sup>5</sup> The “slab total mass” is defined as the integrated mass over the entire analysis region at a given vertical grid level.

the relationship between lofted drops, large precipitation ice mass, and the CG lightning flash rate. The evolution of the vertical distribution of precipitation mass in Fig. 9 clearly demonstrates that Hector was dominated by warm rain microphysical processes prior to 0245 (also see Fig. 3a). The absence of CG lightning before 0300 despite substantial quantities of warm rain is consistent with the requirement for large precipitation-sized ice in the charge separation process leading to significant electric fields and lightning (e.g., Takahashi 1978b; Dye et al. 1986, 1989; Williams 1989; among many others). Despite some earlier reports of lightning in warm clouds (e.g., Foster 1950; Pietrowski 1960; Moore et al. 1960; Lane-Smith 1971), the absence of warm rain CG lightning is consistent with many recent radar and in situ studies of this phenomenon (e.g., Takahashi 1978b; Chauzy et al. 1985; Selvam et al. 1991; Mikhailovsky et al. 1991; Rutledge et al. 1992; Petersen et al. 1996).

After 0245, the convection became sufficiently vigorous to loft drops, providing a source of precipitation-sized ice via drop freezing. As discussed earlier relative to Figs. 2b, 3b, and 7a,c, the first CG flashes occurred at 0300 following the development of significant ice mass in the mixed-phase region. As Hector continued to develop and increase in horizontal size and vertical extent (cf. Figs. 2a–f; 3a,b; 4a) via the merger process (Simpson et al. 1993), peaks in the graupel mass (Fig. 9) between the heights of 0° and  $-20^{\circ}\text{C}$  were associated with rapid increases and maxima in the cloud-to-ground flash rate (e.g., 0315–0330, 0345–0415, and 0433–0515). The effect of the merger process on the production of large ice and CG lightning will be explored further in section 3e. Note that Hector continued to loft supercooled drops up to the height of the  $-10^{\circ}$  to  $-20^{\circ}\text{C}$  temperature range during the entire CG producing period. The continual presence of supercooled raindrops above the freezing level was likely the result of the continuous development of distinct updrafts within new deep cumulonimbi, resulting from the collision of the westward propagating gust front and existing cumulus convection along the sea breeze (Keenan et al. 1994b; Wilson et al. 1999, manuscript submitted to *Mon. Wea. Rev.*).

Each of these new cells in the multicell Hector thus provided a new source of lofted drops. The first cells that penetrated into quiescent air containing no ice particles lofted drops to temperatures as cold as  $-15^{\circ}$  to  $-20^{\circ}\text{C}$  as inferred from  $Z_{\text{dr}}$  and  $K_{\text{dp}}$  (e.g., Figs. 7a,b, 9). Although the supercooled raindrops froze more rapidly when the updrafts carrying them penetrated into existing ice cloud, there was always at least one new updraft carrying supercooled drops to  $-10^{\circ}\text{C}$  or colder (e.g., Fig. 9). This is in contrast to the Florida storm studied by Yuter and Houze (1995), in which  $Z_{\text{dr}}$  data indicated that the precipitation at upper levels was nearly glaciated early in the life cycle of the multicellular convective complex. The difference between the two multicell storms is unclear. We can speculate that more of Hector's

nascent updrafts penetrated into cloud-free air because they triggered along the intersection of a horizontally extensive sea breeze front and a gust front that tended to advect ahead of existing convection (Carbone et al. 2000). Or perhaps, the low-level to midlevel updrafts lofting the supercooled raindrops in Hector may have been more intense than in the Florida storms.

These lofted drops likely froze and quickly rimed, providing a rapid and plentiful source of graupel particles for charge separation via the NIC mechanism. The initial descent of the graupel mass usually triggered pulses in the CG lightning flash rate. This correlation between descending precipitation ice and CG lightning for tropical island convection is similar to prior results for thunderstorms throughout the globe (e.g., Workman and Reynolds 1949; Goodman et al. 1988; Williams et al. 1989; Carey and Rutledge 1996; Petersen et al. 1996; López and Aubagnac 1997). Cloud-to-ground lightning may be initiated by the descent of graupel below the level of main negative charge where the process of charge reversal microphysics causes these ice particles to charge positively (e.g., Jayaratne et al. 1983; Williams et al. 1989; Carey and Rutledge 1996). This lower positive charge may result in the electrical bias that allows for the transfer of negative charge to ground in CG lightning as first suggested by Clarence and Malan (1957).

As shown in Fig. 9, the graupel mass continued its descent below the freezing level where it melted between 3 and 5 km. After sufficient time for gravitational sedimentation (e.g., 15–20 min, assuming  $V_i = 5 \text{ m s}^{-1}$  and a fall from the 5–6.5-km region), a peak in the rain flux (Fig. 8) and rain mass (Fig. 9) reached near the surface (actually 0.5 km in the gridded data). This tendency for peak rainfall near the surface to lag the maximum cloud-to-ground lightning flash rate by 15–20 min is also consistent with past studies of subtropical and midlatitude convection (e.g., Goodman et al. 1988; Carey and Rutledge 1996).

The freezing of supercooled drops may actually enhance cloud electrification in three ways: 1) providing an instantaneous and abundant source of precipitation-sized ice as discussed above, 2) promoting favorable conditions for secondary ice processes via the shattering of freezing drops (e.g., Pruppacher and Klett 1997) or rime splintering (e.g., Hallet and Mossop 1974), and 3) increasing the buoyancy and hence updraft speed of the air parcel via the latent heat of fusion. As noted in Koenig (1963) and reviewed in Young (1993), most observations of enhanced ice crystal concentrations were obtained in cumulus clouds that contained large supercooled drops. Ice enhancements can be an order of magnitude or more (up to  $10^4$ ) for the ice multiplication mechanisms mentioned above (Pruppacher and Klett 1997). According to the NIC mechanism, an order of magnitude increase in the ice crystal concentration would result in an order of magnitude increase in graupel electrification. The increase in buoyancy associated

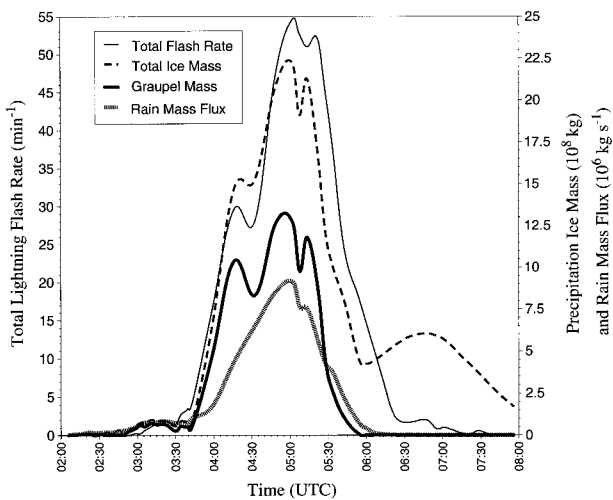


FIG. 10. Evolution of the total lightning flash rate ( $\text{min}^{-1}$ ), total ice mass ( $10^8 \text{ kg}$ ), graupel ice mass ( $10^8 \text{ kg}$ ), and rain mass flux ( $10^6 \text{ kg s}^{-1}$ ) within 40 km of the flat plate antenna. See appendix C for the definitions of and methods for determining total ice and graupel ice mass.

with drop freezing could be significant. For example, peak mixing ratios of supercooled rainwater at  $-5$  to  $-10^\circ\text{C}$  in lightning producing cells were typically  $3\text{--}5 \text{ g kg}^{-1}$  (cf. Figs. 5a, 7b), which might have corresponded to  $1\text{--}1.7$  degrees of extra buoyancy if all the water froze.

### c. Relationship between the total lightning flash rate and precipitation

The presence of a flat plate antenna at the C-pol radar during MCTEX provided us the opportunity to analyze the coevolution of the radar-inferred precipitation structure and the total lightning flash rate (total = IC + CG) within 40 km of the radar. These results complement the islandwide-scale data discussed in the previous section, which focused on the coevolving precipitation fields and CG lightning. In Fig. 10, we present the total lightning flash rate, the total mixed-phase ( $0^\circ$  to  $-40^\circ\text{C}$ ) ice mass, the integrated mixed-phase graupel mass, and the rain mass flux for the entire life cycle (0200–0800). A time–height cross section of the total slab ( $\text{kg km}^{-1}$ ) ice mass versus the 15-min total lightning flash rate is shown in Fig. 11.

During the dominance of warm rain convection prior to 0225 (cf. Figs 2a, 3a, 10, 11), there was no detected lightning activity. The increase in the total ice mass above the height of  $-5^\circ\text{C}$  was associated with the first lightning flashes from 0230 to 0300. The total lightning flash rate, total ice mass, and graupel mass all dramatically increased from 0315 to 0415 associated with the merger process (cf. Figs. 2b,c; 10; 11). The role of the merger process in the production of mixed phase ice mass, rainfall, and lightning will be investigated further in section 3e. As shown in Fig. 10, the total lightning flash rate and total mixed-phase ice mass are well cor-

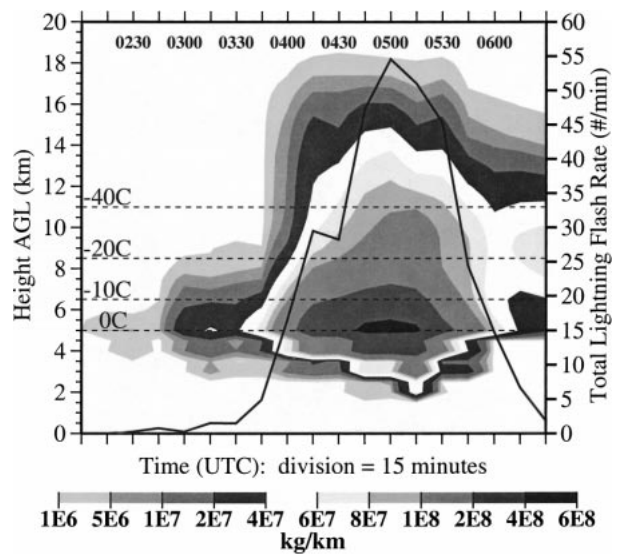


FIG. 11. Time–height cross section of slab total precipitation sized ice mass ( $\text{kg km}^{-1}$ , shaded) within 40 km of the C-pol radar from 0200 to 0630 UTC. The total lightning flash rate ( $\text{min}^{-1}$ , solid line) during this period is repeated for direct comparison.

related ( $\rho = 0.93$ ). The three primary peaks in the total lightning flash rate (0416, 0502, 0522) were either preceded by or coincident with maxima in the total ice mass (0416, 0502, 0514; Fig. 10). As presented in Fig. 11, these peaks in the total lightning flash rate were also accompanied by upward perturbations in the height of the slab ice mass and large temporal gradients of the slab ice mass in the  $0^\circ$  to  $-40^\circ\text{C}$  region. The overall maxima in the mean<sup>6</sup> total lightning flash rate of  $55 \text{ min}^{-1}$  at 0502 was coincident with the absolute peak in the total ice mass and graupel mass (Figs. 10 and 11). As Hector weakened from 0515 to 0615 within 40 km of the radar (cf. Figs. 2d,e; 10; 11), the total lightning flash rate dropped precipitously along with the total ice and graupel masses. This decrease in ice mass was most dramatic in the mixed-phase zone and was also accompanied by downward perturbations in the height of the ice mass (Fig. 11).

The correlation between total ice mass and the total lightning flash rate documented here is similar to previous observations of subtropical and midlatitude thunderstorms (e.g., Larsen and Stansbury 1974; Stansbury et al. 1978; Marshall and Radhakant 1978; Goodman et al. 1988; Carey and Rutledge 1996) and is consistent with a charging mechanism that relies on ice–ice collisions in the presence of supercooled cloud water for particle-scale charge separation (e.g., Takahashi 1978a; Jayaratne et al. 1983; Saunders et al. 1991; among others).

<sup>6</sup> The total lightning flash rate was averaged over the temporal resolution of the radar data (4–15 min). The maximum 1-min average was  $60 \text{ min}^{-1}$ , occurring at 0454 and 0458.

Interestingly, the total ice mass tracked the total flash rate from first lightning until about 0600 when Hector began to dissipate near the radar and visually glaciate, and the total lightning flash rate decreased to  $<10 \text{ min}^{-1}$ . As seen in Figs. 10 and 11, the total ice mass began to increase after 0600 in the  $-15^\circ$  to  $-30^\circ\text{C}$  region and experienced a secondary maxima at 0645 while the total flash rate continued to decrease. We speculate that this sudden disconnect between the total ice mass and the total lightning flash rate is related to the transition from vigorous updraft (i.e., convective) to weak updraft or downdraft (i.e., stratiform), the subsequent loss of cloud water, and the fallout of large precipitation-sized ice. Indeed, graupel and frozen drops were nonexistent after about 0555 within 40 km of the radar (Fig. 10). The lack of large ice and possibly cloud water, both necessary ingredients in the NIC mechanism, could have rendered the electrical generator ineffective despite the presence of smaller, precipitation-sized ice.

The finescale temporal evolution of the rain mass flux shown in Fig. 10 does not match some of the undulations (i.e., relative minima and maxima) seen in the total lightning flash rate and mixed-phase total ice mass (Fig. 10). However, the rain flux does envelope the total lightning flash rate. Indeed, the two quantities are very well correlated ( $\rho = 0.94$ ). As a matter of fact, comparison with section 3b suggests that the integrated rain flux is actually better correlated with the total lightning flash rate than with the CG lightning flash rate.

#### d. Relationship between the surface electric field and precipitation

In this section, we compare the polarimetric radar inferred precipitation structure of a portion of Hector that passed within 20 km of the radar (cf. Figs. 2a–e), to field mill observations of the surface electric field and total lightning flash rate from 0200 to 0630. In addition, the ALDF network was used to isolate the ground discharges associated with this convection. The results are synthesized in Fig. 12, which depicts the temporal evolution of the total ice and rain masses in the vertical, the surface electric field, the total lightning flash rate, and time of occurrence of each CG lightning flash.

The premerger stage (0200–0245) was dominated by warm rain processes as can be seen by the lack of significant ice mass and supercooled water above  $0^\circ\text{C}$  (Fig. 12). This slab water mass is associated with a warm rain cell that was located to the east–northeast of the radar (Fig. 2a) and characterized by reflectivities up to 50 dBZ. During this entire time, the field mill indicated a fairweather electric field (e.g., Uman 1987) of  $60\text{--}80 \text{ V m}^{-1}$  and no lightning transients. From 0245 to 0345, distant convection (at ranges of 20–30 km) caused an enhancement in the fairweather field up to  $200 \text{ V m}^{-1}$ . This enhanced fair field was probably caused by a re-

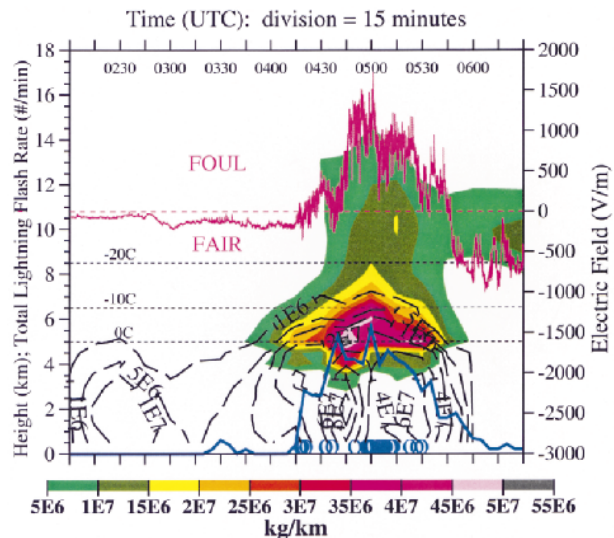


FIG. 12. Evolution of the slab total precipitation sized ice mass ( $\text{kg km}^{-1}$ , color shaded), slab rain mass ( $\text{kg km}^{-1}$ , black dashed contours), surface electric field ( $\text{V m}^{-1}$ , pink line), total lightning flash rate derived from the field mill ( $\text{min}^{-1}$ , thick solid blue line), and the time of occurrence for CG lightning as depicted by the symbol "O" within 20 km of the C-pol radar from 0200 to 0630 UTC.

versal of the sign of the surface electric field associated with a distant thunderstorm dipole (i.e., the so-called field reversal distance; Uman 1987). Distant lightning was registered by the field mill from 0325 to 0345 while the vertical component of the surface electric ( $E$ )-field was still fair and there was little in the way of convection within 20 km of the radar (e.g., Fig. 2b).

From 0345 to 0415, new cells developed to the north of the radar at ranges less than 20 km, along a gust front on the southern side of Hector (Fig. 2c). Aided by convergence along the gust front, these vigorous new cells lofted drops above the freezing level and began the production of precipitation-sized ice (Fig. 12). Within 10 to 15 min of precipitation ice production above  $-10^\circ\text{C}$ , the surface electric field began to increase rapidly toward foul (i.e., positive) values and the first lightning transient was recorded by the field mill at 0415. The first couple of ground discharges occurred 5–10 min later. The positive slope of the surface electric field corresponds well with the increase in the amount and height of the ice mass from 0415 to 0430. The presence of supercooled drops colder than  $-10^\circ\text{C}$  during this time suggests that drop freezing was a major source of precipitation-sized ice for subsequent riming and cloud electrification via the NIC mechanism.

Between 0430 and 0445, a weak excursion in the electric field from a foul field to a near-zero and slightly negative (i.e., fair)  $E$  field was followed by a maximum in the rain mass near the surface (Fig. 12). The field excursion associated with precipitation (FEAWP; Moore and Vonnegut 1977) began (peaked) about 15 (7) min prior to the maximum rainfall near the surface at 0445.

TABLE 1. Average properties of instantaneously occurring features for the 28 Nov 1995 case.

Average feature property	Single-cell features	Merged features	Ratio of merged to single-cell features
Number	10.1 (55%)	8.1 (45%)	0.8
Echo area (km <sup>2</sup> )	86.3 (7%)	1155.9 (93%)	13.4
Rain flux (10 <sup>6</sup> kg s <sup>-1</sup> )	0.28 (3%)	8.62 (97%)	30.8
CG lightning flash rate (min <sup>-1</sup> )	0.0 (0%)	2.0 (100%)	∞
Mixed-phase graupel mass (10 <sup>7</sup> kg)	1.26 (3%)	35.18 (97%)	27.9

The  $E$  field recovered to pre-FEAWP values just after the peak in precipitation near the surface. Takahashi (1983) proposed that positive charging of descending graupel particles at warm temperatures via the NIC mechanism ( $T > -10^{\circ}\text{C}$ ; Takahashi 1978a) could explain the FEAWP beneath thunderstorms. As in the mid-latitude storm studied by Carey and Rutledge (1996), the FEAWP in Fig. 12 appears to be associated with the descent of frozen precipitation in the  $0^{\circ}$  to  $-10^{\circ}\text{C}$  region.

As seen in Fig. 12, the surface electric field increased from  $100\text{ V m}^{-1}$  at 0440 to  $1000\text{--}1500\text{ V m}^{-1}$  by 0500. During the same time, isosurfaces of total ice mass extended vertically (cf.  $E$ -field trace to the  $1 \times 10^7\text{ kg km}^{-1}$  isosurface in Fig. 12) and the amount of integrated mixed-phase (e.g., 5–11 km) ice mass increased. Supercooled drops were continually lofted above the height of  $-10^{\circ}\text{C}$ , as depicted in the contours of slab rain mass in Fig. 12. The freezing of these drops undoubtedly provided a source of large precipitation-sized ice as the cell developed and became more electrified, as will be shown below.

As the cell began to dissipate after 0530, the lofting of supercooled drops stopped and hence the production of large precipitation ice ceased (Fig. 12). As the remaining large precipitation-sized ice fell out of the storm from 0530 to 0545, the field switched from positive to negative polarity (i.e., from predominately negative to positive charge aloft). The onset of this so-called end of storm oscillation (Moore and Vonnegut 1977) in the surface  $E$  field following the fallout of large precipitation-sized ice suggests that the large precipitation-sized ice carried the negative charge to the ground with residual positive charge remaining aloft (Fig. 12). The advection of this storm farther away from the field mill, past the so-called field reversal distance (e.g., Uman 1987) may have also contributed to the reduction and eventual switch in polarity of the surface  $E$  field. After 0545, the  $E$  field remained fair, CG lightning ceased, and the total lightning flash rate continued to decrease toward zero. The remaining ice mass between  $-20^{\circ}$  and  $-40^{\circ}\text{C}$  during this time was likely associated with ice crystals in the anvil. The implication in Fig. 12 is that the large precipitation-sized ice particles were the predominate negative charge carriers while ice crystals in the anvil at 10 km and higher were the predominate positive charge carriers, consistent with the NIC theory. Combining this inference with the discussion of the

FEAWP above, we find the observations summarized in Fig. 12 to be consistent with the classic thunderstorm tripole reviewed in Williams (1989).

#### e. Role of the merger process

In their investigation of the cumulus merger process over the Tiwi Islands, Simpson et al. (1993) determined that 90% of the rainfall beneath a typical Hector comes from merged systems as defined in section 2. Using C-pol radar and ALDF data, we extend the Simpson et al. (1993) results to include the role of the merger process in the production of mixed-phase graupel mass and cloud-to-ground lightning in addition to rainfall and echo area.

The results are summarized in Table 1. Merged convective features in this Hector accounted for 93% of the echo area, 97% of the rainfall, 97% of the mixed phase graupel mass, and 100% of the cloud-to-ground lightning production over the Tiwi Islands, despite representing the minority of convective features (45%). In this event, there were typically more single-cell than merged features despite the fact that merged features accounted for over an order of magnitude more instantaneous echo area in the mean. The average merged convective feature produced approximately 30 times more rainfall and mixed-phase ice mass than the mean single-cell feature. It is important to point out that the increase in rain flux and ice mass cannot be explained simply by the factor of 13 increase in echo area. The merger process actually *enhances* the production of ice mass and rainfall by a factor of 2–3 above the increase in echo area. This enhancement in the mixed-phase ice mass and rainfall is correlated with the production of moderate cloud-to-ground lightning flash rates ( $2\text{ min}^{-1}$  per merged system).

These tendencies are consistent with past merger results in subtropical (Simpson and Woodley 1971; Simpson et al. 1980), tropical oceanic (Houze and Cheng 1977; DeMott and Rutledge 1998), midlatitude (Changnon 1976), and tropical island (Keenan et al. 1990; Simpson et al. 1993) convection. In summary, these studies found that merged systems are larger, taller, more intense, and produce more rainfall than single-cell convection. We extend these results with the additional finding that the merger process significantly enhances the production of mixed-phase ice mass and cloud-to-ground lightning in addition to the rain flux.

As discussed by Westcott (1984), many interactions could occur to cause this net effect. At one end of the spectrum, individual vertical drafts may combine to form one dynamic entity. At the other end, cloud masses may spread out and combine with no dynamic or microphysical consequences. In an intermediate scenario, convective cells may be bridged by cloudy air, still maintain their individual identities, yet interact dynamically and microphysically such that their growth, mature, and decay stages are altered from what they would have been had they remained isolated. With wider cloud bases, merged systems favor the development of more intense convection because of mutual protection of the cells from dilution by entrainment of drier environmental air. With less dry entrainment, cells within merged systems can efficiently convert more surface-based instability to updraft strength and hence more condensate production and hence more rainfall (see Westcott 1984 for a review).

We favor the intermediate scenario. We suggest that a subsequent effect of the upscale development process is an increase in cold pool area and strength. The increased intensity of low-level forcing and increased frequency of low-level interactions of gust fronts and sea breezes plays an important role in the subsequent development of widespread, deep convection (e.g., Carbone et al. 2000). This process is a positive feedback mechanism that continues until all of the potentially buoyant boundary layer air in the path of the travelling cold pool has been processed.

Lightning flash rates are enhanced by the production of more intense and more frequent deep convective cells by the merger process described above (i.e., more intense updrafts, more cloud liquid water, more ice, more charging, more lightning). Electrification and lightning can also be enhanced in merged systems via an "ice seeding effect." Developing updrafts can merge with a mature complex and penetrate existing cloudy air that already contains high concentrations of ice crystals. The enhanced ice crystal concentrations along the periphery of the buoyant updraft bubble in the merged cell could magnify the charge separation process via the NIC mechanism, which is linearly proportional to the ice crystal concentration (e.g., Takahashi 1978). This enhanced charging would likely lead to amplified lightning flash rates.

It is quite remarkable that single-cell convective features produced *no* detectable CG lightning despite the continual presence of 5–20 isolated cells. Analysis of C-pol radar data suggest that most of these features were either entirely contained below the 0°C isotherm or were otherwise dominated by warm rain microphysics (e.g., Fig. 3a). The simultaneous lack of mixed-phase graupel mass and CG lightning is consistent with the crucial role of graupel in the NIC mechanism. Since our electric field and total lightning flash measurements were limited to within about 20 and 40 km, respectively, of the radar, it is quite possible that some of these single-cell features

were electrified to the point of producing intracloud lightning. However, all of the single-cell features within 20–40 km of the radar produced little mixed-phase ice mass and generated no significant *E*-fields or intracloud lightning (cf. Figs. 2a, 10, 11, and 12 from 0200 to 0245).

On two occasions (around 0345 and 0430), single-cell features produced a significant amount ( $>5 \times 10^7$  kg) of graupel mass in the mixed-phase region. Both of these isolated cells originated along a gust front, explosively developed, and quickly merged with the parent complex before producing any CG lightning. The role of these daughter cells in lightning production cannot be underestimated, however, because their mergers with the parent complex were closely followed by two of the primary peaks in graupel mass and CG lightning production in Hector (cf. Fig. 8, 0345–0415 and 0430–0500). This process was captured by the field mill as depicted in Fig. 12. An earlier single cell along the southern coast sea breeze produced no measurable electric fields or lightning from 0200 to 0245. In contrast, an intense cell along a gust front produced significant ice mass and electric fields before merging with the parent echo after 0400.

These results provide some circumstantial support for one of the earliest merger hypotheses developed from observations (Simpson and Woodley 1971; Simpson et al. 1980) and tested by numerical models (Tao and Simpson 1984, 1989), which suggests the critical role of the downdraft and gust front outflows in cumulus merging. It is interesting to speculate on the differences between those single cells that developed vertically into the mixed-phase zone and produced significant ice mass and electric fields and those that did not. The one-dimensional cloud and electricity modeling study of Hector by Petersen (1997) provides insight into this question. Model results revealed great sensitivity of cloud vertical development and subsequent electrification to the strength and duration of low-level forcing applied in the model. Therefore, it is likely that there was insufficient low-level forcing along the Tiwi Islands' sea breeze fronts on 28 November 1995 to produce vertically developed and CG lightning producing single-cell convection. On the other hand, forcing along certain gust fronts appears to have been more than sufficient to cause explosive convective development before merging with the parent cell. The entrainment of dry air into isolated cumulonimbi may have played a role in their inability to develop into the mixed-phase zone and produce lightning. More observational and modeling work is required to determine conclusively the relative roles of decreased dry entrainment and increased low-level forcing in enhancing the production of precipitation and lightning in merged tropical convection.

#### 4. Summary

As recently stated in MacGorman and Rust (1998), "the available data [on tropical lightning] are sparse so

our understanding should be considered embryonic.” Indeed, one of the primary objectives of the Maritime Continent Thunderstorm Experiment (MCTEX; Keenan et al. 1994a) was to “study cloud electrification mechanisms, especially couplings between ice phase precipitation and the occurrence of strong electric fields and lightning.” MCTEX provided a unique dataset with which to accomplish this objective.

Using the first C-band polarimetric radar (BMRC C-pol) observations of tropical convection, a network of ALDFs, a flat plate antenna, and a field mill, we have demonstrated that lightning production in tropical island convection is critically linked to ice processes. Although a direct causal relationship cannot be established from remote measurements, we have demonstrated a clear correlation between mixed-phase ice mass and lightning in an intense tropical island thunderstorm.

This was accomplished by refining earlier techniques aimed at correlating the surface area of an arbitrary radar reflectivity threshold at some height above the freezing level (the so-called Larsen area; Larsen and Stansbury 1974) to the occurrence of lightning. As in other recent studies (e.g., Bringi et al. 1997; López and Aubagnac 1997), we partitioned the reflectivity into rain and ice components using polarimetric radar. The reflectivity associated with ice was then converted into an estimate of ice mass through application of an appropriate  $Z-M$  equation. We then integrated the radar-inferred ice mass throughout the entire mixed-phase zone for comparison with the surface electric field measured by a field mill, the total lightning flash rate as estimated by a flat plate antenna, and the cloud-to-ground lightning flash rate and location observed by a network of ALDFs.

An equally important goal of this study was to determine the connection between cloud-to-ground lightning and overall storm morphology. For example, we explored the role of the cumulus merger process on the relationship between precipitation and CG lightning. The results presented herein suggest robust relationships between the merger process, rainfall, mixed phase ice mass, and lightning in tropical island thunderstorms.

Specific scientific findings from the study are as follows.

- 1) The 28 November 1995 storm was intense and electrically active. When averaged over 1-min intervals, the total lightning flash rates easily exceeded  $1 \text{ s}^{-1}$  and islandwide CG lightning flash rates reached up to  $11 \text{ min}^{-1}$ . Echo tops penetrated 20 km. The 30-dBZ contour reached up to 18 km in height. Maximum observed reflectivities and rainfall rates exceeded 60 dBZ and  $150 \text{ mm h}^{-1}$ , respectively.
- 2) No significant surface electric fields or lightning were associated with convection dominated by warm rain microphysical processes, despite substantial reflectivities and rainfall rates.
- 3) The surface electric field, the total lightning flash rate, and cloud-to-ground lightning were all highly correlated to the radar-inferred mixed-phase ice mass in time and space. The results were consistent with prior findings from investigations of midlatitude, subtropical, and tropical oceanic convection.
  - (i) The integrated observations are consistent with the noninductive charging (NIC) theory, which relies on collisions between large precipitation-sized ice and smaller ice crystals in the presence of supercooled water.
  - (ii) Cloud-to-ground lightning was associated with the production and subsequent descent of large precipitation-sized ice (graupel and frozen drops) from the  $-10^{\circ}$  to  $-20^{\circ}\text{C}$  region. Peaks in the CG lightning flash rate typically lagged peaks in the graupel mass aloft.
  - (iii) Ground stroke locations clustered beneath maxima in radar-inferred mixed-phase ice mass.
  - (iv) Rainfall was correlated to both the CG and total lightning flash rates.
  - (v) The total lightning flash rate and the total ice mass were highly correlated.
  - (vi) Lightning (both CG and IC) and the surface electric field decreased rapidly during the final dissipative stage of Hector. The lack of large precipitation-sized ice and possibly supercooled cloud water during the decay phase rendered the electrical generator ineffective.
  - (vii) The radar and field mill measurements were generally consistent with the classic tripole model.
- 4) Supercooled raindrops were common in the  $0^{\circ}$  to  $-10^{\circ}\text{C}$  region of this tropical island convection. In lightning producing cells, drops were always lofted to the height of the  $-10^{\circ}\text{C}$  isotherm (6.75 km) and sometimes as cold as  $-20^{\circ}\text{C}$  (8.5 km). Due to the multicell nature of Hector, a continual supply of supercooled rainwater was available in the mixed-phase zone throughout the developing and mature phases. This is in contrast to Yuter and Houze (1995), who found that selected multicell storms in Florida almost completely glaciate early in the storm’s life cycle. We speculate that the updrafts in Hector were either more intense and/or tended to ascend in cloud- (and hence ice-) free air more frequently.
- 5) Frozen drops appear to have played a crucial role in storm kinematics, microphysics, and electrification of Hector. The freezing of supercooled raindrops likely provided (i) an instantaneous and plentiful supply of large precipitation sized ice, (ii) a potential source of secondary ice, and (iii) an enhancement in the updraft via the latent heat of freezing.
- 6) Rainfall, mixed-phase precipitation, and lightning production were enhanced in merged cloud systems relative to single-cell cumulonimbi. In our study, single-cell cumulonimbi did not produce a single detectable CG lightning flash. Merged cells produced

97% of the rainfall and mixed-phase ice mass and 100% of the CG lightning. The cell merger process enhanced the production of mixed-phase ice mass and rainfall by a factor of 2–3 above the associated increase in low-level echo area. This enhancement in precipitation production was well correlated with the production of moderate cloud-to-ground lightning flash rates ( $2 \text{ min}^{-1}$  per merged system on average).

We speculate that wider cloud bases and stronger low-level gust front forcing in merged systems promote the efficient conversion of surface-based instability to updraft strength. Increased updraft strength directly results in more condensate production, particularly in the mixed-phase zone, resulting in more ice mass aloft, rainfall, and lightning. Electrification and lightning may also be enhanced in merged systems via an ice seeding effect. In merged systems, a new updraft may rise through cloudy air that already contains high concentrations of ice crystals. Since the NIC mechanism is linearly proportional to ice crystal concentration, charging and hence lightning would be enhanced.

*Acknowledgments.* We wish to thank Dr. Tom Keenan and Mr. Ken Glasson of the Bureau of Meteorology Research Centre for their work to organize MCTEX and to develop the C-pol radar. Staff at NCAR/Atmospheric Technology Division are also recognized for their technical contributions to C-pol. Personnel at NASA/MSFC (including Dr. Rich Blakeslee, Mr. Jeff Bailey, Dr. William Koshak, Dr. Hugh Christian, and Dr. Steven Goodman) are acknowledged for providing the field mill, ALDF network, and the cloud-to-ground lightning location and timing solutions. We thank Dr. Tom Rickenbach for providing the feature identification algorithms and computer code. We acknowledge Dr. Walt Petersen and Mr. David Ahijevych for their collaboration and insight into Hector. Helpful comments from Dr. Jim Dye, Dr. V. N. Bringi, Dr. Graeme Stephens, and three anonymous reviewers improved the clarity of the manuscript. This research was supported by NASA TRMM Grants NAG5-2692 and NAG5-4754, and NSF Grant ATM-9726464.

## APPENDIX A

### Overview of Procedures for Determining Cloud Electrical Properties

The flat plate-derived total lightning flash rate was computed using a signal-to-noise amplitude ratio technique described in Carey and Rutledge (1996) and is typically compared to radar echo characteristics within 40 km of the instrument. It is important to note that there is no fixed range of operation for the flat plate antenna. The distance across which a field change due to lightning can be detected is a function of the sensitivity of the antenna and the magnitude of the field

change itself (e.g., Uman 1987; MacGorman and Rust 1998). Empirical experience with the flat plate antenna in a variety of convective situations suggests that the maximum range for detecting most flashes is about 40 km (e.g., Carey and Rutledge 1996, 1998). Return strokes were handled by requiring 500 ms to pass before the next signal could be considered a separate flash.

An independent estimate of the total lightning flash rate within about 20 km of the radar was obtained by applying a filtered derivative algorithm (Basseville and Nikiforov 1993) on the 50-Hz surface field mill data. The field mill data were passed through a five-point running mean filter. The temporal derivative of the electric field data was accomplished using a simple finite differencing scheme. If  $|dE/dt|$  was greater than  $400 \text{ V m}^{-1} \text{ s}^{-1}$  for at least 0.1 s, then a lightning flash was tabulated. As in the flat plate algorithm, a gap of 0.5 s between  $E$  field perturbations was required before the next distinct lightning flash was recorded by the field mill.

This  $|dE/dt|$  threshold is well above the instrument noise level determined from inspection of 141 hours of lightning-free field mill data (i.e., no radar echo within 50 km). During the thunderstorm-free periods, over 99.9% of the  $|dE/dt|$  was less than  $40 \text{ V m}^{-1} \text{ s}^{-1}$ . In an independent test, the automated algorithm compared favorably to a subjective, visual determination of lightning flash rate.

The field mill estimate of the surface electric field is calibrated and accurate to within  $4 \text{ V m}^{-1}$ . The effective range for detecting the surface electric field and associated lightning transients is approximately 20 km (Uman 1987). Of course, the actual range over which the surface electric field can be detected is dependent on the sensitivity of the field mill, the strength of the in-cloud  $E$  field, and the amount of space charge present in the vicinity of the field mill (e.g., Standler and Winn 1979). Occasionally, transients from a particularly vigorous lightning flash can be detected in the surface electric field at ranges as distant as 25 km. In this study, we adapt the convention that a positive surface electric field corresponds to an upward directed electric field vector (the so-called foul field characterized by net negative charge aloft).

A linear analytic inversion algorithm (Koshak et al. 2000) was utilized on CG data from the network of four ALDFs to retrieve estimates of return stroke location and time of occurrence. Over the Tiwi Islands, Koshak et al. (2000) estimate lightning location retrieval errors of about 0.1–1 km for a four-station solution and 5–10 km for a three-station solution. For the purpose of this study, the location accuracy is sufficient to assign a particular ground stroke to a given convective cell. The retrieved CG return *strokes* were combined into cloud-to-ground lightning *flashes* using a temporal and spatial clustering algorithm similar to that described in Cummins et al. (1998).

APPENDIX B

**Estimation of the Reflectivity Associated with Rain in Mixed-Phase Precipitation**

As reviewed in Doviak and Zrnić (1993), there are two polarimetric radar methods by which the horizontal reflectivity associated with rain can be estimated in mixed-phase precipitation (i.e., a mixture of rain and ice): a power-based method utilizing the difference reflectivity,  $Z_{dp} = 10 \log(Z_h - Z_v)$  (Golestani et al. 1989), and a phase-based method utilizing the specific differential phase,  $K_{dp}$  (Balakrishnan and Zrnić 1990). Both methods rely on the well-known behavior of equilibrium rain drop shape with size (e.g., Pruppacher and Beard 1970). Scattering simulations have demonstrated that the horizontal reflectivity associated with rain is linearly proportional to  $Z_{dp}$  (Golestani et al. 1989) and the natural logarithm of  $K_{dp}$  (Balakrishnan and Zrnić 1990).

These methods assume that precipitation-sized ice particles (i.e., graupel, hail, and frozen drops) tend to be more spherically symmetrical or tumble (e.g., Pruppacher and Klett 1997). Deviations from the assumption of sphericity are mitigated by the significantly lower dielectric constant of ice (e.g., Seliga and Bringi 1976; Herzegh and Jameson 1992). As a result, ice particles contribute to the horizontal reflectivity and vertical reflectivity equally ( $Z_h \approx Z_v$ ) such that  $Z_{dp}$  would be due solely to the presence of rain. Similarly, the specific differential phase of ice is approximately zero such that  $K_{dp}$  is only sensitive to the rain in the radar resolution volume (Balakrishnan and Zrnić 1990). Therefore, the rain reflectivity in mixed-phase precipitation can be estimated directly from either  $Z_{dp}$  or  $K_{dp}$  without being significantly biased by the presence of ice. As discussed in appendix C, the horizontal reflectivity associated with ice in mixed-phase precipitation can then be estimated as a residual difference of the observed  $Z_h$  and estimated  $Z_h(\text{rain})$ .

The  $Z_{dp}$  method has been utilized to estimate latent heating rates associated with precipitation (Chandrasekar et al. 1991; Tong et al. 1998), to investigate microphysical processes within isolated convection (Takahashi et al. 1996) and hailstorms (Meischner et al. 1991; Conway and Zrnić 1993), and to explore the relationship between precipitation and cloud electrification (Carey and Rutledge 1996; Bringi et al. 1997). Similarly, Carey

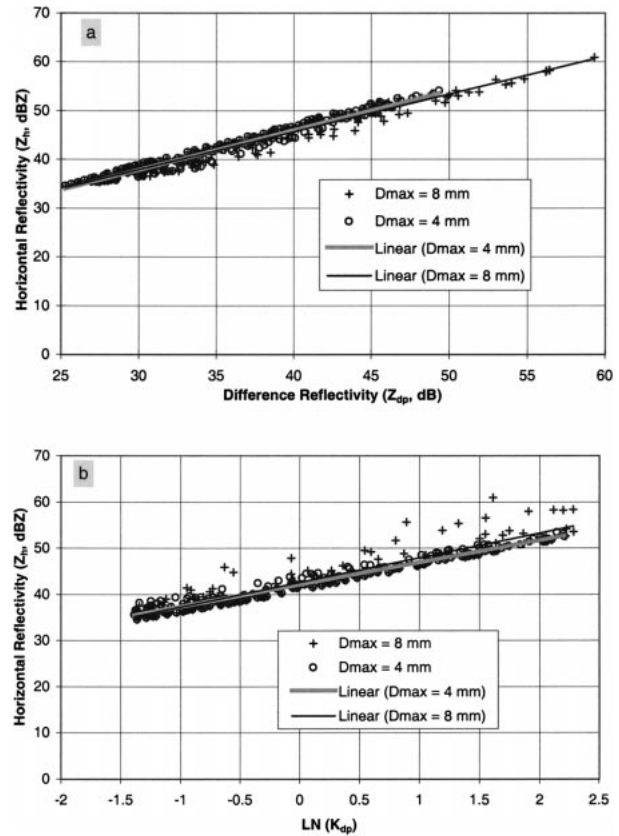


FIG. B1. Scatterplots of the horizontal reflectivity ( $Z_h$ , dBZ) vs (a) the difference reflectivity ( $Z_{dp}$ , dB) and (b) the natural logarithm of the specific differential phase ( $K_{dp}$ ,  $^{\circ} \text{ km}^{-1}$ ) in rainfall as derived from scattering simulations described in Carey et al. (2000). To investigate the effect of large drops on the accuracy of the  $Z_h(Z_{dp})$  and  $Z_h(K_{dp})$  relationships, scatterplots from simulation runs using  $D_{\text{max}} = 4$  mm ( $\circ$ ) and 8 mm ( $+$ ) are shown. A least squares regression line for each simulation run is plotted (4 mm: thick/light line; 8 mm: narrow/dark line). The associated regression equation, coefficient of correlation, and standard error for each regression line is given in Table B1.

TABLE B1. Equations for estimating the horizontal reflectivity associated with rain as derived from scattering simulations.

Equation	Standard error (dBZ)	$\rho^2$
$D_{\text{max}} = 4$ mm		
$Z_h(Z_{dp}) = 0.822Z_{dp} + 13.09$	0.93	0.966
$Z_h(K_{dp}) = 4.817 \ln(K_{dp}) + 42.11$	0.93	0.965
$D_{\text{max}} = 8$ mm		
$Z_h(Z_{dp}) = 0.776Z_{dp} + 14.59$	1.07	0.969
$Z_h(K_{dp}) = 5.314 \ln(K_{dp}) + 42.57$	1.96	0.892

and Rutledge (1996, 1998) and López and Aubagnac (1997) have used the  $K_{dp}$  method to investigate hail microphysics and the relationship between precipitation and lightning. With the exception of Meischner et al. (1991), all of the above studies utilized S-band radar observations. Ours is the first study to employ these methods with C-band observations of tropical convection. In addition, there has been little critical intercomparison of the two methods. Therefore, we explored the relative performance of each procedure to estimate the horizontal reflectivity associated with rain in tropical convection at C band using both scattering simulations and C-pol observations taken during MCTEX.

Incomplete gamma size distributions were fit to disdrometer observations of tropical rainfall collected during MCTEX (Keenan et al. 1999, manuscript submitted to *J. Appl. Meteor.*). Using these gamma size distributions as input to a scattering model (Carey et al.

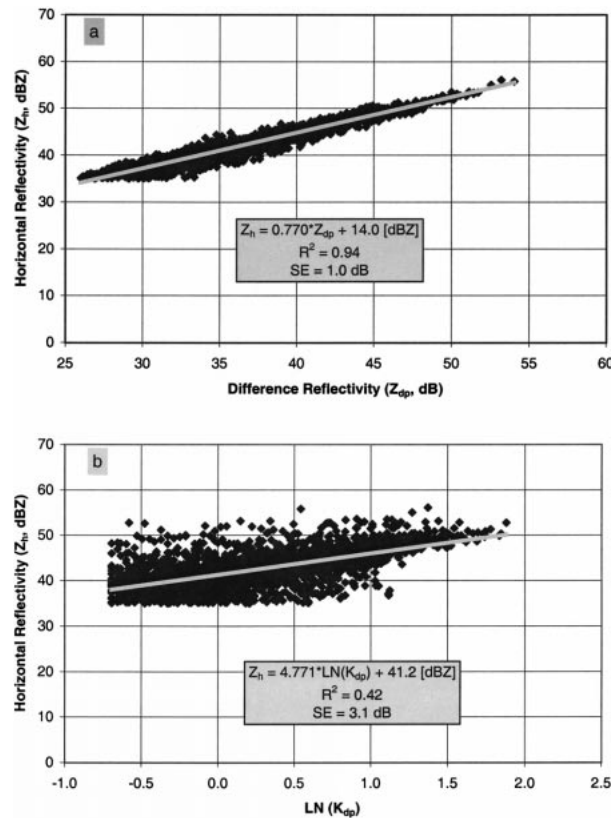


FIG. B2. Scatterplots of the horizontal reflectivity ( $Z_h$ , dBZ) vs (a) the difference reflectivity ( $Z_{dp}$ , dB) and (b) the natural logarithm of the specific differential phase ( $K_{dp}$ ,  $^{\circ} \text{ km}^{-1}$ ) obtained from C-pol radar observations of tropical rainfall at 1 km AGL on 28 November 1995 from 0344 to 0433 UTC. A least squares regression line for each empirical dataset is shown along with the associated equation, coefficient of correlation, and the standard error.

2000), we calculated the  $Z_h(Z_{dp})$  and  $Z_h(K_{dp})$  relationships (Table B1) in rain using a least squares regression procedure. Given the relatively small sample volume of disdrometers, the lack of information regarding the distribution of drops  $>5.4$  mm, the C-pol observations of

large  $Z_{dr}$  (3–5 dB), and videosonde observations of drops up to 8 mm in diameter during MCTEX (Carey et al. 2000), we felt that it was necessary to explore various options to obtain physically realistic parameterizations for  $D_{max}$  in the polarimetric scattering calculations. In this study, we choose to conduct a sensitivity study that explored the extremes of 4 mm and 8 mm for  $D_{max}$ . More detailed sensitivity studies of the large drop tail at C band were recently conducted by Zrnich et al. (2000) and Keenan et al. (1999, manuscript submitted to *J. Appl. Meteor.*). The resulting  $Z_h(\text{rain})$  versus  $Z_{dp}$  and  $\ln(K_{dp})$  scatterplots as a function of maximum drop size are presented in Figs. B1a and B1b, respectively. The standard error for both  $Z_h(Z_{dp})$  and  $Z_h(K_{dp})$  are about 0.9 dB for  $D_{max} = 4$  mm. When the maximum drop size is increased to 8 mm, the scatter for the  $Z_h(K_{dp})$  relationship increases significantly (Fig. B1a) while the  $Z_h(Z_{dp})$  scatter remains about the same (Fig. B1b). This is reflected in a factor of 2 increase of the standard error of the  $Z_h(K_{dp})$  estimator when  $D_{max}$  is increased from 4 to 8 mm (Table B1). In the presence of large drops, the difference reflectivity is clearly superior to the specific differential phase in estimating the horizontal reflectivity associated with rain.

The above simulations did not include the effects of measurement error. As demonstrated in Fig. B1a, Table B1, and prior studies (e.g., Tong et al., 1998),  $Z_h$  is highly correlated to  $Z_{dp}$  in rainfall. Hence, the scatter between  $Z_h$  and  $Z_{dp}$  was not significantly perturbed by the addition of simulated measurement error. In contrast, the addition of  $0.4^{\circ} \text{ km}^{-1}$  of standard measurement error to  $K_{dp}$  in the above scattering simulation increases the standard error of the  $Z_h(K_{dp})$  estimator to 2.3 dBZ (3 dBZ) for  $D_{max} = 4$  mm (8 mm). Clearly,  $Z_h(Z_{dp})$  is more immune to measurement error than  $Z_h(K_{dp})$ .

To support these simulation results and also to derive unbiased relationships for rain reflectivity in MCTEX convection, we utilized C-pol radar data at 1 km above ground level (AGL) from 0344 to 0433 UTC on 28 November 1995 to derive empirical  $Z_h(Z_{dp})$  and  $Z_h(K_{dp})$  relationships in rainfall using least squares regression.

TABLE B2. Evaluation of the empirical  $Z_h(Z_{dp})$  equation using observed data from other days, times, and altitudes during MCTEX.

$Z_h(Z_{dp})$ (dBZ)	Test 1 <sup>a</sup>			Test 2 <sup>b</sup>			Test 3 <sup>c</sup>		
	N	Bias <sup>d</sup> (dB)	SE <sup>e</sup> (dB)	N	Bias (dB)	SE (dB)	N <sup>d</sup>	Bias (dB)	SE (dB)
All $Z_h$	3744	−0.29	1.05	6624	−0.27	0.95	5432	+0.29	1.03
$35 \leq Z_h < 40$	901	+0.28	1.05	1471	+0.23	1.01	1721	+0.93	1.01
$40 \leq Z_h < 45$	1469	−0.20	0.92	2646	−0.20	0.84	2401	+0.17	0.84
$45 \leq Z_h < 50$	1168	−0.76	1.01	2026	−0.63	0.92	1276	−0.33	0.93
$50 \leq Z_h < 55$	192	−0.76	0.71	446	−0.66	0.67	34	+0.31	0.37

<sup>a</sup> Test 1: 28 Nov 95, 1 km, 0330, 0334, 0339, 0449, 0502, 0508 UTC.

<sup>b</sup> Test 2: 28 Nov 95, 2.5 km, 0330, 0334, 0339, 0449, 0502, 0508 UTC.

<sup>c</sup> Test 3: 23 Nov 95, 1 km, 0640–0645 UTC.

<sup>d</sup> The bias =  $\sum (Z_e - Z_o)/N$ , where  $Z_e$  is the estimated reflectivity,  $Z_o$  is the observed or “true” reflectivity, and  $N$  is the number of samples.

<sup>e</sup> The standard error,  $SE = [\sum (Z_e - \bar{Z}_e - Z_o + \bar{Z}_o)^2/N]^{1/2}$ . The overbar indicates a mean. For  $N < 100$ , the SE was multiplied by  $\sqrt{N/(N-3)}$ .

TABLE B3. Evaluation of the empirical  $Z_h(K_{dp})$  equation using observed data from other days, times, and altitudes during MCTEX.

$Z_h(K_{dp})$ (dBZ)	Test 1			Test 2			Test 3		
	N	Bias (dB)	SE (dB)	N	Bias (dB)	SE (dB)	N	Bias (dB)	SE (dB)
All $Z_h$	3744	-0.48	2.88	6624	-1.18	3.11	5432	+0.35	2.69
$35 \leq Z_h < 40$	901	+2.59	2.19	1471	+2.37	2.24	1721	+2.58	2.55
$40 \leq Z_h < 45$	1469	-0.56	1.97	2646	-1.06	1.92	2401	-0.19	1.89
$45 \leq Z_h < 50$	1168	-2.00	1.92	2026	-2.83	2.12	1276	-1.44	1.87
$50 \leq Z_h < 55$	192	-4.34	2.67	446	-5.34	2.83	34	-6.41	2.06

All grid points that satisfied  $Z_h \geq 35$  dBZ,  $Z_{dr} > 0.25$  dB, and  $K_{dp} > 0.4^\circ \text{ km}^{-1}$  were included in the regression sample. The resulting  $Z_h(Z_{dp})$  and  $Z_h(K_{dp})$  scatterplots and regression results are given in Figs. B2a, and B2b, respectively. As expected,  $Z_h$  is highly correlated to  $Z_{dp}$  in rain (e.g., 94% of the variance explained). In contrast, only 41% of the variance in  $Z_h$  is explained by  $\ln(K_{dp})$  in C-pol observations of rainfall. The standard error (SE) of the empirically derived  $Z_h(K_{dp})$  estimator is a factor of 3 higher than the SE of  $Z_h(Z_{dp})$  (Figs. B2a,b). The empirically derived  $Z_h(Z_{dp})$  relationship appears to be superior to  $Z_h(K_{dp})$ .

To evaluate the stability of these empirically derived  $Z_h$  estimators in rain at different altitudes, times, and days, three independent test samples were compiled from C-pol radar observations during MCTEX and compared to the regression equations in Figs. B2a,b. The bias and standard error in dB for  $Z_h(Z_{dp})$  and  $Z_h(K_{dp})$  were calculated for each complete test sample ( $Z_h \geq 35$  dBZ) and for four separate subsamples every 5 dBZ for each test dataset (Tables B2 and B3, respectively). The results are consistent among the three different test samples. The standard error for  $Z_h(Z_{dp})$  is consistently around 1 dB, compared to 2–3 dB for  $Z_h(K_{dp})$ . The overall sample bias for both estimators was small ( $< 0.5$  dB) in all three tests. However, the bias for  $Z_h(K_{dp})$  in individual subsamples was often very large (2–6 dB). Comparatively, biases in the  $Z_h(Z_{dp})$  subsamples were typically very small (0.2–0.9 dB).

Based on the empirical and simulation results above, we have chosen to use  $Z_{dp}$  over  $K_{dp}$  to estimate the reflectivity associated with rain in mixed-phase precipitation since the  $Z_h(Z_{dp})$  estimator 1) is less affected by the presence of large drops and measurement error, 2) has a significantly smaller standard error and bias, and 3) provides stable results in rainfall at different heights, times, and days.

## APPENDIX C

### Equations for Estimating the Rain and Ice Mass from C-Band Polarimetric Radar Data

In this section, we review a method of inverting rain and ice mass from observed C-band polarimetric radar quantities. As derived and evaluated in appendix B

above, the difference reflectivity ( $Z_{dp}$ , dB) (Golestani et al. 1989) is first used to estimate directly the contribution of rain to the horizontal reflectivity ( $Z_h$ , dBZ):

$$Z_h^{\text{rain}} = 0.77Z_{dp} + 14.0 \quad (\text{dBZ}). \quad (\text{C1})$$

An estimate of the rain mass ( $M_w$ ) is then obtained from the following  $Z$ - $M$  relationship:

$$M_w = 3.01 \times 10^{-4} (Z_H^{\text{rain}})^{0.846} \quad (\text{g kg}^{-1}), \quad (\text{C2})$$

where the units of  $Z_H(\text{rain})$  are in  $\text{mm}^6 \text{ m}^{-3}$ . Equation (C2) above was developed using a curve fitting procedure on simulated radar data of rain over the Tiwi Islands. In order to create the simulated rainfall data, observations of drop size distributions taken during MCTEX with a disdrometer (Keenan et al. 1999, manuscript submitted to *J. Appl. Meteor.*) were used as input to the T-matrix scattering model (Barber and Yeh 1975), assuming C band (5.33 cm),  $T = 20^\circ\text{C}$ , a maximum drop diameter of 8 mm, and an equilibrium drop shape versus size relationship (Green 1975).

The contribution of ice to the horizontal reflectivity can then be calculated as a residual from

$$Z_H^{\text{ice}} = Z_H - Z_H^{\text{rain}} \quad (\text{mm}^6 \text{ m}^{-3}), \quad (\text{C3})$$

where  $Z_H$  is the observed horizontal reflectivity. With this estimate of  $Z_H(\text{ice})$ , we then calculate the precipitation-sized ice mass ( $M_{\text{ice}}$ ) using a relationship based on the Rayleigh approximation,<sup>7</sup>

$$M_{\text{ice}} = 1000\pi \left( \frac{\rho_i}{\rho_a} \right) N_0^{3/7} \left( \frac{5.28 \times 10^{-18} Z_H^{\text{ice}}}{720} \right)^{4/7} \quad (\text{g kg}^{-1}), \quad (\text{C4})$$

where  $Z_H(\text{ice})$  is in  $\text{mm}^6 \text{ m}^{-3}$ ,  $\rho_i$  is the ice density ( $\text{kg m}^{-3}$ ),  $\rho_a$  is the air density ( $\text{kg m}^{-3}$ ), and  $N_0$  ( $\text{m}^{-4}$ ) is the intercept parameter of an assumed inverse exponential distribution for ice. For simplicity's sake, we utilize a fixed intercept parameter ( $N_0 = 4 \times 10^6 \text{ m}^{-4}$ ) that is taken from a bulk-microphysical cloud modeling

<sup>7</sup> Equation (C4) was obtained by combining the classic Rayleigh expressions for  $Z$  and  $M$ . For simplicity, an infinite inverse exponential size distribution was assumed. The analytical solutions for  $Z$  and  $M$  for an inverse exponential distribution are given in Doviak and Zrníć (1993).

study of tropical convection over the Tiwi Islands (Petersen 1997). Also for simplicity's sake, we assume a constant ice density of solid ice at 0°C (0.917 kg m<sup>-3</sup>). We utilized (C4) because no suitable  $Z$ - $M$  relationship could be identified in the literature for ice within the convective portion of a deep, tropical island thunderstorm.

Clearly, the actual values of  $N_0$  and  $\rho_i$  likely differed from these simplified assumptions and likely varied in time and space as Hector evolved through its life cycle. Therefore, our estimate of ice mass from  $Z_h(\text{ice})$  should be considered a gross estimate that is proportional to and is within about a factor of 2 of the actual ice mass (assuming a factor of 2 and 2 variability in  $N_0$  and  $\rho_i$ , respectively). Since *trends* in the storm integrated ice mass (e.g., relatively low vs relatively high precipitation ice mass) as they relate to electric field and lightning characteristics are key to the interpretations and conclusions of this study, this approach was deemed to be sufficient for our purposes.

The standard error of the rain reflectivity estimate using the  $Z_{dp}$  method (C1) is approximately 1 dB (see appendix B). As a result, we require that  $Z_h - Z_h(\text{rain}) > 1$  dB below the melting level in order to accurately estimate the residual  $Z_h(\text{ice})$ . Otherwise, we set  $Z_H(\text{rain}) = Z_H$  and  $Z_H(\text{ice}) = 0$  mm<sup>6</sup> m<sup>-3</sup>. Similarly, if  $Z_h - Z_h(\text{ice}) < 1$  dB above the freezing level, then  $Z_H(\text{ice}) = Z_H$  and  $Z_H(\text{rain}) = 0$  mm<sup>6</sup> m<sup>-3</sup>.

It is important to note that  $Z_{dp}$  can be used to differentiate between rain and ice only if  $Z_h$  is sufficiently large (i.e., diameter  $\geq 1$  mm) such that rain is characterized by significant oblateness (e.g., Green 1975). Based on the scattering properties of typical drop size distributions for convection over the Tiwi Islands (Keenan et al. 1999, manuscript submitted to *J. Appl. Meteor.*) and an equilibrium drop shape versus size relationship (Green 1975), we have utilized the  $Z_{dp}$  rain-ice partitioning method [(C1)–(C4)] if  $Z_h \geq 35$  dBZ. In this case, (C4) would yield the graupel mass,  $M_g$ , associated primarily with large precipitation-sized ice (e.g., graupel, frozen drops, and large aggregates). If  $Z_h < 35$  dBZ above the -10°C level, we then assume that  $Z_H(\text{ice}) = Z_H$  in (C4), which would now be associated primarily with ice crystals and small aggregates, since horizontal reflectivity is proportional to  $D^6$ . In this study, we will consider both the ice mass associated with large ice or graupel mass ( $Z_h > 35$  dBZ,  $M_g$ ) and the total ice mass ( $M_i$ ) that includes echoes of all reflectivities. Below the 0°C level, we assume that reflectivity echoes characterized by  $Z_h < 35$  dBZ are dominated by rain.

#### APPENDIX D

##### C-Band Rain-Rate Equations

Using results of the C-band scattering simulations described in Carey et al. (2000), we derived rain-rate

estimators customized to the drop size distributions (DSDs) observed during MCTEX based on  $Z_h$ ,  $K_{dp}$ ,  $Z_h/Z_{dr}$ , and  $K_{dp}/Z_{dr}$  using a least squares curve fitting procedure. The corresponding equations for the four radar rainfall estimators, (D1)–(D4), are summarized in Table D1 along with coefficient of correlations and normalized standard errors of the estimators. The curve-fitting samples for the rainfall estimators utilizing either  $K_{dp}$  or  $Z_{dr}$  were restricted by the standard error of the measurement, which are 0.25 dB for  $Z_{dr}$  and 0.4° km<sup>-1</sup> for  $K_{dp}$  (Keenan et al. 1998). Note that the statistical errors listed in Table D1 do not include measurement error.

An optimal polarimetric radar-based rain mass flux algorithm (e.g., Jameson 1991; Chandrasekar et al. 1993) over the Tiwi Islands (kg s<sup>-1</sup>), which utilized the best available estimator of the four rain-rate relationships (D1)–(D4) at each point, was applied after the data was corrected for propagation effects. As shown in Jameson (1991) and Ryzhkov and Zrnić (1995b) and confirmed in our study, the standard errors of the polarimetric radar rain estimators decrease significantly from (D1) to (D4). In other words, the  $SE[R(Z_h)] > SE[R(K_{dp})] > SE[R(Z_h, Z_{dr})] > SE[R(K_{dp}, Z_{dr})]$  as shown in Table D1. As in Ryzhkov and Zrnić (1995b), we determined that the statistical error of the  $R(K_{dp}, Z_{dr})$  estimator is three times less than the SE of the  $R(Z_h, Z_{dr})$  estimator. Therefore, the composite rain mass flux algorithm first used (D4) if possible. The  $R(K_{dp}, Z_{dr})$  estimator was used at a grid point if  $K_{dp} \geq 0.4^\circ$  km<sup>-1</sup> and  $Z_{dr} \geq 0.25$  dB. If  $K_{dp} < 0.4^\circ$  km<sup>-1</sup> (or was missing) and  $Z_{dr} \geq 0.25$  dB, then the composite rain mass flux algorithm utilized  $R(Z_h, Z_{dr})$  (D3) at the grid point. In the event that  $Z_{dr} < 0.25$  dB or was missing and  $K_{dp} \geq 0.4^\circ$  km<sup>-1</sup> at a grid point, the algorithm used the  $R(K_{dp})$  estimator (D2). Finally, if none of the above constraints were met, the mass flux algorithm used  $R(Z_h)$  (D1) at the point in question. After applying this selection algorithm to the four rain-rate estimators at each point over the entire grid, the selected rain rates (mm h<sup>-1</sup>) were averaged and then converted from a depth of water over the grid area per unit time to a mass flux (kg s<sup>-1</sup>) by assuming a density of 1000 kg m<sup>-3</sup> for water.

TABLE D1. Equations for C-band polarimetric radar rain-rate estimators.

Rain-rate estimator ( $R$ , mm h <sup>-1</sup> )*	$\rho$	Normalized standard error (NSE)**
D1. $R(Z_h) = 5.865 \times 10^{-3} Z_h^{0.862}$	0.965	193%
D2. $R(K_{dp}) = 23.37 K_{dp}^{0.82}$	0.951	41%
D3. $R(Z_h, Z_{dr}) = 1.783 \times 10^{-3} Z_h^{0.983} Z_{dr}^{-1.24}$	0.999	24%
D4. $R(K_{dp}, Z_{dr}) = 25.00 K_{dp}^{0.988} Z_{dr}^{-0.583}$	0.972	8%

\* Note:  $Z_h$  in mm<sup>6</sup> m<sup>-3</sup>,  $Z_{dr}$  in dB, and  $K_{dp}$  in deg km<sup>-1</sup>.

\*\* NSE =  $[\Sigma (R_e - \bar{R}_e - R_i + \bar{R}_i)^2/n]^{1/2}/\bar{R}_e$ , where  $R_e$  is the estimated rain rate,  $R_i$  is the true rain rate, the overbar indicates a mean, and  $n$  is the number of samples.

## REFERENCES

- Atlas, D. A., 1966: The balance level in convective storms. *J. Atmos. Sci.*, **23**, 635–651.
- Austin, P. M., and A. C. Bemis, 1950: A quantitative study of the “bright band” in radar precipitation echoes. *J. Meteor.*, **7**, 145–151.
- Balakrishnan, N., and D. S. Zrnić, 1990: Estimation of rain and hail rates in mixed-phase precipitation. *J. Atmos. Sci.*, **47**, 565–583.
- Barber, P., and C. Yeh, 1975: Scattering of electromagnetic waves by arbitrarily shaped dielectric bodies. *Appl. Opt.*, **14**, 2864–2872.
- Basseville, M., and I. V. Nikiforov, 1993: *Detection of Abrupt Changes: Theory and Application*. Prentice Hall, 528 pp.
- Blyth, A. M., R. E. Benestad, P. R. Krehbiel, and J. Latham, 1997: Observations of supercooled raindrops in New Mexico summertime cumuli. *J. Atmos. Sci.*, **54**, 569–575.
- Bringi, V. N., and A. Hendry, 1990: Technology of polarization diversity radars for meteorology. *Radar in Meteorology: Battan Memorial and 40th Anniversary Radar Meteorology Conference*, D. Atlas, Ed., Amer. Meteor. Soc., 153–190.
- , V. Chandrasekar, N. Balakrishnan, and D. S. Zrnić, 1990: An examination of propagation effects on radar measurements at microwave frequencies. *J. Atmos. Oceanic Technol.*, **7**, 829–840.
- , L. Liu, P. C. Kennedy, V. Chandrasekar, and S. A. Rutledge, 1996: Dual multiparameter radar observations of intense convective storms: The 24 June 1992 case study. *Meteor. Atmos. Phys.*, **59**, 3–31.
- , K. Knupp, A. Detwiler, L. Liu, I. J. Caylor, and R. A. Black, 1997: Evolution of a Florida thunderstorm during the Convection and Precipitation/Electrification Experiment: The case of 9 August 1991. *Mon. Wea. Rev.*, **125**, 2131–2160.
- Carbone, R. E., J. W. Wilson, T. D. Keenan, and J. Hacker, 2000: Tropical island convection in the absence of significant topography. Part I: Life cycle of diurnally formed convection. *Mon. Wea. Rev.*, in press.
- Carey, L. D., and S. A. Rutledge, 1996: A multiparameter radar case study of the microphysical and kinematic evolution of a lightning producing storm. *Meteor. Atmos. Phys.*, **59**, 33–64.
- , and —, 1998: Electrical and multiparameter radar observations of a severe hailstorm. *J. Geophys. Res.*, **103**, 13 979–14 000.
- , —, D. A. Ahijevych, and T. D. Keenan, 2000: Correcting propagation effects in C-band polarimetric radar observations of tropical convection using differential propagation phase. *J. Appl. Meteor.*, in press.
- Chandrasekar, V., C. A. Atwater, and T. H. Vonder Haar, 1991: Convective latent heating estimates from radar data. Preprints, *25th Int. Conf. on Radar Meteorology*, Paris, France, Amer. Meteor. Soc., 155–158.
- , E. Gorgucci, and G. Scarchilli, 1993: Optimization of multiparameter radar estimates of rainfall. *J. Appl. Meteor.*, **32**, 1288–1293.
- Changnon, S. A., Jr., 1976: Effects of urban areas and echo merging on radar echo behavior. *J. Appl. Meteor.*, **15**, 561–570.
- Chauzy, S., M. Chong, A. Delannoy, and S. Despiau, 1985: The June 22 tropical squall line observed during COPT 81 experiment: Electrical signatures associated with dynamical structure and precipitation. *J. Geophys. Res.*, **90**, 6091–6098.
- Clarence, N. D., and D. J. Malan, 1957: Preliminary discharge processes in lightning flashes to ground. *Quart. J. Roy. Meteor. Soc.*, **83**, 161–172.
- Conway, J. W., and D. S. Zrnić, 1993: A study of embryo production and hail growth using dual-Doppler and multiparameter radars. *Mon. Wea. Rev.*, **121**, 2511–2528.
- Cooper, W. A., 1974: Possible mechanism for contact nucleation. *J. Atmos. Sci.*, **31**, 1832–1837.
- Cummins, K. L., M. J. Murphy, E. A. Bardo, W. L. Hiscox, R. B. Pyle, and A. E. Pifer, 1998: A combined TOA/MDF technology upgrade of the U.S. National Lightning Detection Network. *J. Geophys. Res.*, **103**, 9035–9044.
- DeMott, C. A., and S. A. Rutledge, 1998: The vertical structure of TOGA COARE convection. Part I: Radar echo distributions. *J. Atmos. Sci.*, **55**, 2730–2747.
- Doviak, R. J., and D. S. Zrnić, 1993: *Doppler Radar and Weather Observations*. 2d ed. Academic Press, 562 pp.
- Dye, J. E., J. J. Jones, W. P. Winn, T. A. Cerni, B. Gardiner, D. Lamb, R. L. Pitter, J. Hallett, and C. P. R. Saunders, 1986: Early electrification and precipitation development in a small, isolated Montana cumulonimbus. *J. Geophys. Res.*, **91**, 1231–1247.
- , W. P. Winn, J. J. Jones, and D. W. Breed, 1989: The electrification of New Mexico thunderstorms, 1. Relationship between precipitation development and the onset of electrification. *J. Geophys. Res.*, **94**, 8643–8656.
- Foster, H., 1950: An unusual observation of lightning. *Bull. Amer. Meteor. Soc.*, **31**, 140–141.
- French, J. R., J. H. Helsdon, A. G. Detwiler, and P. L. Smith, 1996: Microphysical and electrical evolution of a Florida thunderstorm, 1. Observations. *J. Geophys. Res.*, **101**, 18 961–18 978.
- Golestani, Y., V. Chandrasekar, and V. N. Bringi, 1989: Intercomparison of multiparameter radar measurements. *Proc. 24th Conf. on Radar Meteorology*, Tallahassee, FL, Amer. Meteor. Soc., 309–314.
- Goodman, S. J., D. E. Buechler, P. D. Wright, and W. D. Rust, 1988: Lightning and precipitation history of a microburst-producing storm. *Geophys. Res. Lett.*, **15**, 1185–1188.
- Green, A. W., 1975: An approximation for the shape of large raindrops. *J. Appl. Meteor.*, **14**, 1578–1583.
- Hallett, J., and S. C. Mossop, 1974: Production of secondary ice crystals during the riming process. *Nature*, **249**, 26–28.
- Herzogh, P. H., and A. R. Jameson, 1992: Observing precipitation through dual-polarization radar measurements. *Bull. Amer. Meteor. Soc.*, **73**, 1365–1374.
- Houze, R. A., Jr., and C.-P. Cheng, 1977: Radar characteristics of tropical convection observed during GATE: Mean properties and trends over the summer season. *Mon. Wea. Rev.*, **105**, 964–980.
- Hubbert, J., and V. N. Bringi, 1995: An iterative filtering technique for the analysis of copolar differential phase and dual-frequency radar measurements. *J. Atmos. Oceanic Technol.*, **12**, 643–648.
- Illingworth, A. J., J. W. Goddard, and S. M. Cherry, 1987: Polarization radar studies of precipitation development in convective storms. *Quart. J. Roy. Meteor. Soc.*, **113**, 469–489.
- Jameson, A. R., 1985: Deducing the microphysical character of precipitation from multiple-parameter radar polarization measurements. *J. Climate Appl. Meteor.*, **24**, 1037–1047.
- , 1991: A comparison of microwave techniques for measuring rainfall. *J. Appl. Meteor.*, **30**, 32–54.
- , and D. B. Johnson, 1990: Cloud microphysics and radar. *Radar in Meteorology: Battan Memorial and 40th Anniversary Radar Meteorology Conference*, D. Atlas, Ed., Amer. Meteor. Soc., 323–340.
- , M. J. Murphy, and E. P. Krider, 1996: Multiple-parameter radar observations of isolated Florida thunderstorms during the onset of electrification. *J. Appl. Meteor.*, **35**, 343–354.
- Jayarathne, E. R., C. P. R. Saunders, and J. Hallett, 1983: Laboratory studies of the charging of soft hail during ice crystal interactions. *Quart. J. Roy. Meteor. Soc.*, **109**, 609–630.
- Keenan, T. D., B. R. Morton, X. S. Zhang, and K. Nyguen, 1990: Some characteristics of thunderstorms over Bathurst and Melville Islands near Darwin, Australia. *Quart. J. Roy. Meteor. Soc.*, **116**, 1153–1172.
- , and Coauthors, 1994a: Science Plan—Maritime Continent Thunderstorm Experiment. BMRC Research Report 44, 61 pp. [Available from BMRC, P.O. Box 1289K, Melbourne, Victoria 3001, Australia.]
- , B. Ferrier, and J. Simpson, 1994b: Development and structure of a maritime continent thunderstorm. *Meteor. Atmos. Phys.*, **53**, 185–222.
- , K. Glasson, F. Cummings, T. S. Bird, J. Keeler, and J. Lutz, 1998: The BMRC/NCAR C-band polarimetric (C-POL) radar system. *J. Atmos. Oceanic Technol.*, **15**, 871–886.

- Koenig, L. R., 1963: The glaciating behavior of small cumulonimbus clouds. *J. Atmos. Sci.*, **20**, 29–47.
- Koshak, W. J., R. J. Blakeslee, and J. C. Bailey, 2000: Data retrieval algorithms for validating the Optical Transient Detector and the Lightning Imaging Sensor. *J. Atmos. Oceanic Technol.*, **17**, 279–297.
- Krider, E. P., R. C. Noggle, and M. A. Uman, 1976: A gated wideband magnetic direction finder for lightning return strokes. *J. Appl. Meteor.*, **15**, 301–306.
- Lane-Smith, D. R., 1971: A warm thunderstorm. *Quart. J. Roy. Meteor. Soc.*, **97**, 577–578.
- Larsen, H. R., and E. J. Stansbury, 1974: Association of lightning flashes with precipitation cores extending to height 7 km. *J. Atmos. Terr. Phys.*, **36**, 1547–1553.
- López, R. E., and J.-P. Aubagnac, 1997: The lightning activity of a hailstorm as a function of changes in its microphysical characteristics inferred from polarimetric radar observations. *J. Geophys. Res.*, **102**, 16 799–16 813.
- MacGorman, D. R., and W. D. Rust, 1998: *The Electrical Nature of Storms*. Oxford University Press, 422 pp.
- Malan, D. J., and B. F. J. Schonland, 1950: An electrostatic fluxmeter of short response-time for use in studies of transient field-changes. *Proc. Phys. Soc. London Ser. B*, **63**, 402–408.
- Marshall, J. S., and S. Radhakant, 1978: Radar precipitation maps as lightning indicators. *J. Appl. Meteor.*, **17**, 206–212.
- Meischner, P. F., V. N. Bringi, D. Heimann, and H. Höller, 1991: A squall line in southern Germany: Kinematics and precipitation formation as deduced by advanced polarimetric and Doppler radar measurements. *Mon. Wea. Rev.*, **119**, 678–701.
- Mikhailovsky, Y., Y. Agapov, and B. Koloskov, 1992: Electrification of the tropical clouds. *Proc. Ninth Int. Conf. on Atmos. Electricity*, St. Petersburg, Russia, International Commission of Atmospheric Electricity, 176–178.
- Mohr, C. G., 1986: Merger of mesoscale data sets into a common Cartesian format for efficient and systematic analyses. *J. Atmos. Oceanic Technol.*, **3**, 143–161.
- Moore, C. B., and B. Vonnegut, 1977: The thundercloud. *Lightning*, Vol. 1, R. H. Golde, Ed., Academic Press, 51–98.
- , B. Vonnegut, B. A. Stein, and H. J. Survillas, 1960: Observations of electrification and lightning in warm clouds. *J. Geophys. Res.*, **65**, 1907–1910.
- Petersen, W. A., 1997: Multi-scale process studies in the tropics: Results from lightning observations. Ph.D. dissertation, Colorado State University, 354 pp.
- , S. A. Rutledge, and R. E. Orville, 1996: Cloud-to-ground lightning observations from TOGA COARE: Selected results and lightning location algorithms. *Mon. Wea. Rev.*, **124**, 602–620.
- , R. C. Cifelli, S. A. Rutledge, B. S. Ferrier, and B. F. Smull, 1999: Shipborne dual-Doppler operations during TOGA COARE: Integrated observations of storm kinematics and electrification. *Bull. Amer. Meteor. Soc.*, **80**, 81–96.
- Pietrowski, E. L., 1960: An observation of lightning in warm clouds. *J. Meteor.*, **17**, 562–563.
- Pruppacher, H. R., and K. V. Beard, 1970: A wind tunnel investigation of the internal circulation and shape of water drops falling at terminal velocity in air. *Quart. J. Roy. Meteor. Soc.*, **96**, 247–256.
- , and J. D. Klett, 1997: *Microphysics of Clouds and Precipitation*. 2d ed. Kluwer Academic, 954 pp.
- Ramachandran, R. A. Detwiler, J. Helsdon Jr., P. L. Smith, and V. N. Bringi, 1996: Precipitation development and electrification in Florida thunderstorm cells during Convection and Precipitation/Electrification Project. *J. Geophys. Res.*, **101**, 1599–1620.
- Rickenbach, T. M., and S. A. Rutledge, 1998: Convection in TOGA COARE: Horizontal scale, morphology, and rainfall production. *J. Atmos. Sci.*, **55**, 2715–2729.
- Rutledge, S. A., E. R. Williams, and T. D. Keenan, 1992: The Down Under Doppler and Electricity Experiment (DUNDEE): Overview and preliminary results. *Bull. Amer. Meteor. Soc.*, **73**, 3–16.
- Ryzhkov, A., and D. S. Zrnić, 1995a: Precipitation and attenuation measurements at a 10-cm wavelength. *J. Appl. Meteor.*, **34**, 2121–2134.
- , and —, 1995b: Comparison of dual-polarization radar estimators of rain. *J. Atmos. Oceanic Technol.*, **12**, 249–256.
- Saunders, C. P. R., W. D. Keith, and R. P. Mitzeva, 1991: The effect of liquid water content on thunderstorm charging. *J. Geophys. Res.*, **96**, 11 007–11 017.
- Seliga, T. A., and V. N. Bringi, 1976: Potential use of radar differential reflectivity measurements at orthogonal polarizations for measuring precipitation. *J. Appl. Meteor.*, **15**, 69–76.
- Selvam, A. M., R. Vijayakumar, G. K. Manohar, and A. S. R. Murty, 1991: Electrical, microphysical, and dynamical observations in summer monsoon clouds. *Atmos. Res.*, **26**, 19–32.
- Simpson, J., and W. L. Woodley, 1971: Seeding cumulus in Florida: New 1970 results. *Science*, **176**, 117–126.
- , N. E. Westcott, R. J. Clerman, R. A. Pielke, 1980: On cumulus mergers. *Arch. Meteor. Geophys. Bioklimatol. Ser. A*, **29**, 1–40.
- , T. D. Keenan, B. Ferrier, R. H. Simpson, and G. J. Holland, 1993: Cumulus mergers in the maritime continent region. *Meteor. Atmos. Phys.*, **51**, 73–99.
- Smith, P. L., D. J. Musil, A. G. Detwiler, and R. Ramachandran, 1999: Observations of mixed-phase precipitation within a CaPE thunderstorm. *J. Appl. Meteor.*, **38**, 145–155.
- Solomon, R., and M. Baker, 1994: Electrification of New Mexico thunderstorms. *Mon. Wea. Rev.*, **122**, 1878–1886.
- Standler, R. B., and W. P. Winn, 1979: Effects of corona on electric fields beneath thunderstorms. *Quart. J. Roy. Meteor. Soc.*, **105**, 285–302.
- Stansbury, E. J., and J. S. Marshall, 1978: Sferics at two stations compared with radar-observed precipitation. *Atmos.–Ocean*, **16**, 281–292.
- Steiner, M., R. A. Houze Jr., and S. E. Yuter, 1995: Climatological characterization of three-dimensional storm structure from operational radar and rain gauge data. *J. Appl. Meteor.*, **34**, 1978–2007.
- Takahashi, N., H. Uyeda, and K. Kikuchi, 1996: Evolution process and precipitation particles of an isolated echo observed with dual-polarization Doppler radar near Sapporo on July 9, 1992. *J. Fac. Sci. Hokkaido Univ., Ser. VII (Geophys.)*, **10**, 135–153.
- Takahashi, T., 1978a: Riming electrification as a charge generation mechanism in thunderstorms. *J. Atmos. Sci.*, **35**, 1536–1548.
- , 1978b: Electrical properties of oceanic tropical clouds at Ponape, Micronesia. *Mon. Wea. Rev.*, **106**, 1598–1612.
- , 1983: Electric structure of oceanic tropical clouds and charge separation processes. *J. Meteor. Soc. Japan*, **61**, 656–669.
- Tao, W.-K., and J. Simpson, 1984: Cloud interactions and merging: numerical simulations. *J. Atmos. Sci.*, **41**, 2901–2917.
- , and —, 1989: A further study of cumulus interactions and mergers: Three-dimensional simulation with trajectory analyses. *J. Atmos. Sci.*, **46**, 2974–3004.
- Tong, H., V. Chandrasekar, K. R. Knupp, and J. Stalker, 1998: Multiparameter radar observations of time evolution of convective storms: Evaluation of water budgets and latent heating rates. *J. Atmos. Oceanic Technol.*, **15**, 1097–1109.
- Uman, M. A., 1987: *The Lightning Discharge*. Academic Press, 377 pp.
- Vonnegut, B., 1994: The atmospheric electricity paradigm. *Bull. Amer. Meteor. Soc.*, **75**, 53–61.
- Westcott, N., 1984: A historical perspective on cloud mergers. *Bull. Amer. Meteor. Soc.*, **65**, 219–226.
- Williams, E. R., 1989: The tripole structure of thunderstorms. *J. Geophys. Res.*, **94**, 13 151–13 167.
- , M. E. Weber, and R. E. Orville, 1989: The relationship between lightning type and convective state of thunderclouds. *J. Geophys. Res.*, **94**, 13 213–13 220.
- , S. A. Rutledge, S. C. Geotis, N. Renno, E. Rasmussen, and T. Rickenbach, 1992: A radar and electrical study of tropical hot towers. *J. Atmos. Sci.*, **49**, 1386–1395.

- Workman, E. J., and S. E. Reynolds, 1949: Electrical activity as related to thunderstorm cell growth. *Bull. Amer. Meteor. Soc.*, **30**, 142–149.
- Young, K. C., 1993: *Microphysical Processes in Clouds*. Oxford University Press, 427 pp.
- Yuter, S. E., and R. A. Houze Jr., 1995: Three-dimensional kinematic and microphysical evolution of Florida Cumulonimbus. Part II: Frequency distributions of vertical velocity, reflectivity, and differential reflectivity. *Mon. Wea. Rev.*, **123**, 1941–1963.
- Zipser, E. J., and K. R. Lutz, 1994: The vertical profile of radar reflectivity of convective cells: A strong indicator of storm intensity and lightning probability? *Mon. Wea. Rev.*, **122**, 1751–1759.
- Znić, D. S., N. Balakrishnan, C. L. Ziegler, V. N. Bringi, K. Aydin, T. Matejka, 1993: Polarimetric signatures in the stratiform region of a mesoscale convective system. *J. Appl. Meteor.*, **32**, 678–693.
- , D. S., T. D. Keenan, L. D. Carey, and P. T. May, 2000: Sensitivity analysis of polarimetric variables at a 5-cm wavelength in rain. *J. Appl. Meteor.*, in press.